Interface Focus

Biomedical photoacoustic imaging

Paul Beard

Interface Focus 2011 **1**, 602-631 first published online 21 June 2011
doi: 10.1098/rsfs.2011.0028

Interface Focus

Interface Focus (2011) **1**, 602–631
doi:10.1098/rsfs.2011.0028
Published online 22 June 2011

Review

Biomedical photoacoustic imaging

Paul Beard*

Department of Medical Physics and Bioengineering, University College London, Gower Street, London WC1E 6BT, UK

Photoacoustic (PA) imaging, also called optoacoustic imaging, is a new biomedical imaging modality based on the use of laser-generated ultrasound that has emerged over the last decade. It is a hybrid modality, combining the high-contrast and spectroscopic-based specificity of optical imaging with the high spatial resolution of ultrasound imaging. In essence, a PA image can be regarded as an ultrasound image in which the contrast depends not on the mechanical and elastic properties of the tissue, but its optical properties, specifically optical absorption. As a consequence, it offers greater specificity than conventional ultrasound imaging with the ability to detect haemoglobin, lipids, water and other light-absorbing chomophores, but with greater penetration depth than purely optical imaging modalities that rely on ballistic photons. As well as visualizing anatomical structures such as the microvasculature, it can also provide functional information in the form of blood oxygenation, blood flow and temperature. All of this can be achieved over a wide range of length scales from micrometres to centimetres with scalable spatial resolution. These attributes lend PA imaging to a wide variety of applications in clinical medicine, preclinical research and basic biology for studying cancer, cardiovascular disease, abnormalities of the microcirculation and other conditions. With the emergence of a variety of truly compelling *in vivo* images obtained by a number of groups around the world in the last 2–3 years, the technique has come of age and the promise of PA imaging is now beginning to be realized. Recent highlights include the demonstration of whole-body small-animal imaging, the first demonstrations of molecular imaging, the introduction of new microscopy modes and the first steps towards clinical breast imaging being taken as well as a myriad of *in vivo* preclinical imaging studies. In this article, the underlying physical principles of the technique, its practical implementation, and a range of clinical and preclinical applications are reviewed.

Keywords: photoacoustic; ultrasound; imaging; medical; biomedical

1. OVERVIEW

Research into the underlying physics of photoacoustic (PA) techniques has a relatively long, if sporadic, history dating back to 1880 when Alexander Graham Bell first discovered the PA effect following his observation of the generation of sound owing to the absorption of modulated sunlight [1]. Thereafter, relatively little active scientific research or technological development took place until the development of the laser in the 1960s which provided the high peak power, spectral purity and directionality that many PA sensing applications require. A raft of industrial and scientific sensing applications then began to emerge in the 1970s and 1980s. However, these applications generally exploited the indirect gas-phase cell type of PA detection, in which acoustic waves propagating in a gas generated by laser-induced surface heating are detected with a microphone [2]. This is in contrast to the direct detection of laser-induced ultrasound waves which biomedical PA imaging exploits. Although the latter direct detection approach was explored for characterizing solids as a potential non-destructive testing tool, it was not until the mid-1990s that it began to be investigated for biomedical imaging and the first images began to appear thereafter [3–9]. This early work, undertaken by a handful of researchers, progressed steadily, if not with any notable degree of rapidity, until the early to mid-2000s when the first truly compelling *in vivo* images began to be obtained. From this point onwards, the field has witnessed major growth in terms of the development of instrumentation, image reconstruction algorithms, functional and molecular imaging capabilities and the *in vivo* application of the technique in clinical medicine and basic biological research. It is this latter period that this review is focused on.

In PA or thermoacoustic imaging, ultrasound waves are excited by irradiating tissue with modulated

*pbeard@medphys.ucl.ac.uk

Electronic supplementary material is available at http://dx.doi.org/10.1098/rsfs.2011.0028 or via http://rsfs.royalsocietypublishing.org.

One contribution of 15 to a Theme Issue 'Recent advances in biomedical ultrasonic imaging techniques'.

Received 23 March 2011
Accepted 13 May 2011

electromagnetic radiation, usually pulsed on a nanosecond timescale although other modulation techniques can be used [10–12]. In PA imaging, optical wavelengths in the visible and near-infrared (NIR) part of the spectrum between 550 and 900 nm are most commonly used. The NIR spectral range 600–900 nm offers the greatest penetration depth extending to several centimetres. Thermoacoustic imaging employs significantly longer wavelengths, beyond the optical spectrum and into the microwave band (300 MHz–3 GHz), and can provide even greater penetration depths. In the case of optical excitation, absorption by specific tissue chromophores such as haemoglobin, melanin, water or lipids followed by rapid conversion to heat produces a small temperature rise (approx. less than 0.1 K)—well below that required to cause physical damage or physiological changes to tissue. This leads to an initial pressure increase, which subsequently relaxes resulting in the emission of broadband (approx. tens of megahertz) low-amplitude (less than 10 kPa) acoustic waves. The latter propagate to the surface where they are detected either by a single mechanically scanned ultrasound receiver or an array of receivers in order to acquire a sequence of A-lines. By measuring the time of arrival of the acoustic waves and knowing the speed of sound, an image can be reconstructed in much the same way that a conventional pulse-echo ultrasound image is formed. Depending on the specific imaging mode (see §4), the recorded A-lines can either be used directly to form an image or alternatively used in conjunction with a reconstruction algorithm based on backprojection or phased array beamforming principles. An important difference between pulse-echo ultrasound (US) and PA image formation, however, is that with the former, localization can be achieved by focusing the transmit beam as well as the receive beam. In PA imaging, for depths beyond approximately 1 mm, the overwhelming optical scattering exhibited by most soft tissues precludes equivalently focusing the 'transmit signal'—the excitation light—for the purpose of localization. In PA imaging, for depths greater than approximately 1 mm, localization can be achieved in reception only. A further difference between PA and US imaging lies in the magnitude of the acoustic pressures involved. Diagnostic clinical US scanners can produce focal peak pressures in excess of 1 MPa, whereas PA pressure amplitudes are several orders of magnitude lower, typically less than 10 kPa. Thus, nonlinear acoustic propagation is not encountered in PA imaging, so there is no PA equivalent of US tissue harmonic imaging. The low PA pressure amplitudes also means that the potential hazards due to US exposure are not of concern—those relating to laser exposure dominate safety-related considerations.

Although PA and US image formation and the factors that affect spatial fidelity and resolution are essentially the same, the sources of image contrast are fundamentally different. An US image provides a representation of the acoustic impedance mismatch between different tissues. US image contrast therefore, depends on the mechanical and elastic properties of tissue. A PA image, however, represents the initial pressure distribution produced by the deposition of the optical energy. With some assumptions, this image can be taken to be proportional to the absorbed optical energy distribution, which depends on the optical absorption and scattering properties of the tissue. In fact, it is the former that dominates and thus PA image contrast is often said to be 'absorption-based'. As a consequence, PA imaging can provide greater tissue differentiation and specificity than US because differences in optical absorption between different tissue types can be much larger than those in acoustic impedance. A case in point is the strong preferential optical absorption of haemoglobin. This makes PA imaging particularly well suited to imaging the microvasculature, which can be difficult to visualize with pulse-echo US owing to the weak echogenicity of microvessels. In addition, the spectral dependence of optical absorption enables image contrast provided by specific tissue chromophores to be selectively enhanced by tuning the laser excitation wavelength to their peak absorption. Thus, for example, the presence of lipid deposits in atheromatous plaques can be revealed by choosing an excitation wavelength coincident with the lipid absorption peak at 1210 nm. The spectroscopic nature of the PA effect can be further exploited to quantify the concentrations of specific chromophores via their spectral signatures to provide physiological parameters. An important example of this is the spectroscopic measurement of blood oxygen saturation (sO_2). By acquiring images at multiple wavelengths and applying a spectroscopic analysis, the known spectral differences in oxyhaemoglobin (HbO_2) and deoxyhaemoglobin (HHb) can be used to quantify their concentrations and thus obtain a measurement of blood sO_2.

However, although the large variation in the optical absorption properties of tissue provides PA imaging with its high contrast, it comes at a cost, namely penetration depth. For example, whilst the strong preferential absorption of haemoglobin is advantageous in terms of contrast, it is also a major contributing factor to the strong optical attenuation exhibited by most tissues. As a consequence, although penetration depths of several centimetres can be achieved, PA imaging is unlikely to ever match the penetration depth limit of ultrasound which can be 10 cm or more in soft tissues. On the other hand, the penetration depth available to PA imaging significantly exceeds that of purely optical imaging techniques such as multiphoton or confocal microscopy that rely on unscattered or so-called ballistic photons. As well as being able to image structure and function via optical absorption and its wavelength dependence, other capabilities of PA imaging include blood flow measurement by exploiting the acoustic Doppler effect in a manner analogous to conventional Doppler US and temperature sensing via the temperature dependence of the PA generation process.

The combination of the strong spectral discrimination arising from optical tissue interactions and the high spatial resolution associated with ultrasound propagation lends PA imaging to a broad range of potential applications in clinical medicine, preclinical research

and biology. The ability to map the structure, oxygenation status and flow characteristics of the vasculature makes PA imaging well suited to the assessment of tumours and other pathologies characterized by abnormalities in the morphology and function of the vasculature. Imaging breast and skin cancers are potential clinical applications that exploit this capability. Others include the assessment of the skin microvasculature for studying superficial soft tissue damage, such as burns or abnormalities of the microcirculation in patients with lower limb venous disease and diabetes. By exploiting the contrast provided by lipid absorption, there is the potential to identify vulnerable plaques prone to rupture in the coronary arteries using an intravascular PA imaging probe in a manner analogous to intravascular ultrasound (IVUS). Other clinical applications lie in opthalmology, high intensity focused ultrasound (HIFU) and photothermal treatment monitoring. PA imaging has a role to play in studying mouse models, which are widely used as a preclinical research platform for studying human disease processes. As well as imaging the anatomy and physiology of small-animal models, PA imaging has strong potential as a preclinical molecular imaging modality through the use of optically absorbing targeted contrast agents or reporter genes that express absorbing proteins.

Several previous review articles on PA imaging, some focusing on specific aspects of the technique such as its role in neuroimaging [13], molecular imaging [14] and miocrovascular imaging [15], as well as more general reviews [16–19] appear in the literature. The aim of this paper is to provide an overview of the underlying physics of PA imaging, its practical implementation, the functional and molecular imaging capability it can provide and the biomedical applications it lends itself to. It is also intended to compare it with conventional ultrasound given the similarities between the two modalities. Thus in §2, consideration is given to the physical properties that underlie PA image contrast and the specific tissue constituents that contribute to it. Section 3 discusses the factors that define penetration depth and spatial resolution. The two principal PA imaging modes and their variants, PA tomography (PAT) and microscopy, are described in §4. The means by which one can go beyond purely structural imaging and provide functional, physiological and molecular information using PA spectroscopy, flowmetry and thermometry are outlined in §5. Finally, a range of current and potential clinical and preclinical imaging applications are described in §6.

2. PHOTOACOUSTIC IMAGE CONTRAST

In order to identify the origins of PA image contrast, it is instructive to consider the PA signal generation process. As described above, pulsed laser light is incident on the tissue surface. Depending on the wavelength, the light penetrates to some depth. In doing so, it is multiply scattered and absorbed, the latter by specific light absorbing molecules known as chromophores. The absorbed laser energy is converted into heat by vibrational and collisional relaxation. This produces an initial pressure increase and the subsequent emission of acoustic waves which propagate to the surface where they are detected. In this way, the signal generation mechanism can be regarded as one in which the optically induced initial pressure distribution p_0 is encoded onto a propagating acoustic wave which, upon detection by an ultrasound receiver located on the surface, is converted to a time-resolved electrical signal. Since the PA image is then formed from a set of such PA signals detected at different spatial points, it follows that the PA image is a representation of p_0. Given this, what physical properties of the tissue does p_0 then depend upon? As might be expected, p_0 is related to the heating produced by the deposited laser energy. If impulsive heating is assumed, and in practice, this requires that the acoustic propagation time is small compared with the length scale of the heated volume, then by simple thermodynamic considerations it can be shown that p_0 at a point r is proportional to the absorbed optical energy $H(r)$ [20]

$$p_0(r) = \Gamma H(r), \tag{2.1}$$

where Γ is known as the Grüneisen coefficient, a dimensionless thermodynamic constant that provides a measure of the conversion efficiency of heat energy to pressure and is given by $\Gamma = \beta c^2/C_\mathrm{p}$ where β is the volume thermal expansivity, c the sound speed and C_p the specific heat capacity at constant pressure. The absorbed optical energy distribution $H(r)$ is given by the product of the local absorption coefficient $\mu_\mathrm{a}(r)$ and the optical fluence $\phi(r;\, \mu_\mathrm{a},\, \mu_\mathrm{s},\, g)$ where μ_a and μ_s are the absorption and scattering coefficients over the illuminated tissue volume and g is the anistropy factor. Writing p_0 explicitly, we obtain

$$p_0(r) = \Gamma \mu_\mathrm{a}(r) \phi(r; \mu_\mathrm{a}, \mu_\mathrm{s}, g). \tag{2.2}$$

As equation (2.2) illustrates, p_0 depends upon a variety of mechanical, thermodynamic and optical parameters. However, in PA imaging, the mechanical and thermodynamic properties are usually considered to vary sufficiently weakly between different tissue types that they can be regarded as being spatially invariant. There are inevitably some limits to this assumption and there is a growing recognition that image contrast provided by certain tissues may in part originate from the heterogeneities in the Grüneisen coefficient [21]. However, this notwithstanding, image contrast can be assumed to be dominated by the optical absorption and scattering properties of the tissue. In fact, it transpires that optical absorption tends to dominate and for this reason PA images are often described as being 'absorption based'. However, it is important to recognize that this does not mean that image contrast is directly proportional to the absorption coefficient μ_a. As equation (2.2) shows, p_0 is proportional to the product of μ_a and the fluence ϕ which is itself dependent on μ_a, so p_0 is a nonlinear function of μ_a. This distinction is of critical importance when considering the spectroscopic capability of the technique as described in §5.1.

The dominance of optical absorption as the primary source of PA image contrast lends PA imaging to the

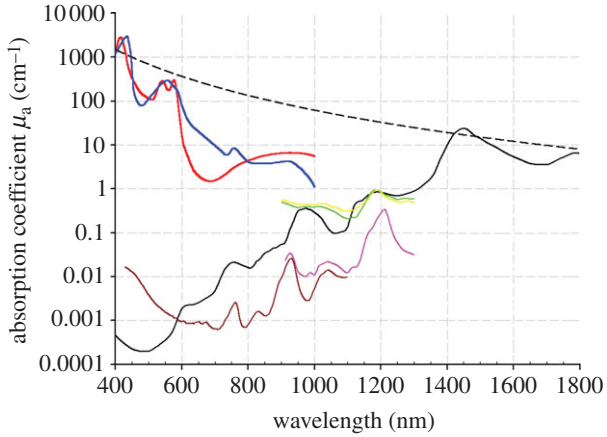

Figure 1. Absorption coefficient spectra of endogenous tissue chromophores. Oxyhaemoglobin (HbO_2), red line: (http://omlc.ogi.edu/spectra/hemoglobin/summary.html; 150 gl^{-1}), deoxyhaemoglobin (HHb), blue line: (http://omlc.ogi.edu/spectra/hemoglobin/summary.html; 150 gl^{-1}), water, black line [22] (80% by volume in tissue), lipid[(a)], brown line [23] (20% by volume in tissue), lipid[(b)], pink line [24], melanin, black dashed line (http://omlc.ogi.edu/spectra/melanin/mua.html; μ_a corresponds to that in skin). Collagen (green line) and elastin (yellow line) spectra from [24].

visualization of anatomical features that contain an abundance of chromophores such as haemoglobin, lipids and water. Of these, haemoglobin is the most important for wavelengths below 1000 nm. As figure 1 shows, between 650 and 900 nm the absorption coefficients of both the oxygenated and deoxygenated states of haemoglobin at physiologically realistic concentrations are at least an order of magnitude higher than the other major chromophores, such as water, lipids and elastin that are present in connective tissues, blood vessels and other organ constituents. At shorter wavelengths extending into the visible part of the spectrum, haemoglobin absorption is even higher and can exceed that of other chromophores by more than two orders of magnitude. It is the very strong preferential absorption of haemoglobin that enables the vasculature to be visualized with such high contrast in PA images. Furthermore, the differences in the absorption spectra of HbO_2 and HHb shown in figure 1 can be exploited to measure blood oxygenation by acquiring images at multiple wavelengths and applying a spectroscopic analysis as described in §5.1. In this way, the absorption-based contrast of PA imaging allows functional as well as structural images of the vasculature to be obtained.

Although melanin has a higher absorption coefficient than blood, it tends to be highly localized in regions, such as the skin or the retina rather than being a major constituent of most tissues. It does not therefore tend to dominate PA image contrast in the way that haemoglobin does. Nevertheless, it forms an important source of contrast for visualizing melanin-rich structures such as certain pigmented lesions in the skin and the retinal-pigmented epithelium (RPE). Absorption by lipids is significantly lower than that of haemoglobin over the visible and NIR range up until around 1100 nm when blood absorption is dominated by water rather than haemoglobin and the strong lipid absorption peak at 1210 nm becomes predominant. This peak can be exploited to image localized lipid deposits such as those found in atherosclerotic plaques.

Chromophores such as haemoglobin and melanin absorb much more strongly than other tissue chromophores and thus provide an obvious source of primary contrast. However, the more weakly absorbing chromophores such as water and lipids which may not be obviously visible on a PA image can still be detected by exploiting their characteristic spectral signatures. This involves the use of spectroscopic inversion or unmixing techniques applied to images acquired at different wavelengths—in much the same way that blood oxygen measurements can be made by exploiting the known spectral differences between HHb and HbO_2. Thus, for example, although the absorption coefficient of water at physiological concentrations in tissue is significantly less than that of haemoglobin over much of the visible and NIR wavelength range, it can still be detected by acquiring images at a range of wavelengths around its absorption peak at 975 nm [25,26] and applying a spectroscopic inversion. The weaker lipid absorption peaks at 920, 970 and 1040 nm can be similarly exploited to provide lipid-based contrast.

As well as endogenous contrast, a variety of targeted contrast agents that absorb at visible and NIR wavelengths can provide additional sources of spectrally selective PA contrast and be used to image disease-specific receptors. These include organic dyes such as indocyanine green (ICG) and methylene blue which can be used clinically in some circumstances or nanostructures such as metallic nanorods or shells which are currently limited to preclinical use. When appropriately targeted, these agents can bind to a disease-specific cellular or intracellular receptor with the spectral signature of the dye/nanostructure providing the source of contrast in the PA image. Nanoparticles of various geometries, in particular, are of major interest as their plasmon resonance absorption cross sections can be orders of magnitude higher than dye molecules. In addition, by adjusting their geometric parameters, their peak absorption wavelength can be tuned to NIR wavelengths where tissue penetration is greatest.

3. PENETRATION DEPTH AND SPATIAL RESOLUTION

3.1. Penetration depth

Penetration depth is limited ultimately by optical and acoustic attenuations. In general, for most soft tissues, although acoustic attenuation is significant, it is optical attenuation that dominates. Optical attenuation depends on both the absorption and scattering coefficients and, as figure 1 would suggest, is strongly wavelength-dependent.

In optically scattering media such as tissues, optical penetration depth is best characterized by the effective attenuation coefficient μ_{eff} derived from diffusion theory where $\mu_{\mathrm{eff}} = (3\mu_a(\mu_a + \mu_s'))^{1/2}$ and μ_a and μ_s' are the absorption and reduced scattering coefficients,

respectively. In homogeneous scattering media, once at a depth beyond several transport mean free paths (approx. 1 mm), the light becomes diffuse and the irradiance decays exponentially with depth with μ_{eff} the exponential constant. $1/\mu_{\mathrm{eff}}$ is therefore the depth at which the irradiance has decreased by $1/e$ and termed the penetration depth. At an excitation wavelength of 700 nm which lies in the spectral region (600–900 nm) where tissue is at its most transparent and using physiologically realistic values of μ_{s} ($1.6\,\mathrm{mm}^{-1}$) and concentrations of HbO_2 and HHb (1% by volume and assuming 95% sO_2), water (74% by volume) and lipids (25% by volume), gives a value of $\mu_{\mathrm{eff}} \sim 0.13\,\mathrm{mm}^{-1}$. The $1/e$ optical penetration depth is thus approximately 8 mm. This means that, once beyond the first millimetre in tissue, light is attenuated by approximately a factor of 4 for each additional centimetre of penetration depth. Assuming a value of $0.75\,\mathrm{dB\,cm^{-1}\,MHz^{-1}}$ for plane wave acoustic attenuation and a frequency of 10 MHz, the total attenuation owing to both optical and acoustic attenuation is thus at least one order of magnitude per centimetre. This represents one of the major challenges in PA imaging as to penetrate several centimetres in tissue incurs a signal attenuation of several orders of magnitude thus requiring the detection of extremely weak ultrasound signals. Despite this, through careful choice of wavelength, optimization of the light delivery, transducer design parameters and signal processing, it has been demonstrated that penetration depths of several centimetres are attainable. A penetration depth of 4 cm has been achieved *in vivo* in the human breast [27] using an excitation wavelength of 800 nm. Other studies using tissue phantoms and *ex vivo* tissues have suggested depths of 5–6 cm may be achievable with the use of contrast agents [28,29]. With regard to the optimum wavelength range, it has been suggested that longer wavelengths, such as 1064 nm, at which blood absorption is low, might provide a penetration depth advantage if contrast agents that absorb at this wavelength are used [30].

3.2. Spatial resolution

In common with pulse-echo US imaging, spatial resolution depends ultimately on the frequency content of the acoustic wave arriving at the detector. In PA imaging, nanosecond excitation laser pulses are most often used and can result in extremely broadband acoustic waves with a frequency content extending to several tens or even hundreds of megahertz, depending on the length scale of the optical absorbers. Under these conditions, the bandwidth of the PA signal and thus the spatial resolution, is not usually limited by the generation process itself. Instead, it is the bandlimiting of the propagating PA wave owing to the frequency-dependent acoustic attenuation exhibited by soft tissues that limits the maximum frequency content of the PA wave and thus defines the ultimate practically achievable spatial resolution limit. Under these circumstances, spatial resolution scales with depth. Acoustic attenuation strongly depends upon tissue type but an approximate rule of thumb is that for centimetre penetration depths, sub-millimetre spatial resolution is possible, decreasing to sub-100 μm for millimetre penetration depths and sub-10 μm spatial resolution for depths of a few hundred micrometres. Although acoustic attenuation defines the ultimate spatial resolution limit, other factors such as detector bandwidth, element size and the area over which the PA signals are recorded—the detection aperture—can be limiting factors in practice. This is particularly so when imaging superficial features that lie within a few millimetres of the surface. The bandwidth of the PA signal can then extend to several tens of megahertz presenting significant challenges in terms of meeting the detection bandwidth and spatial sampling requirements.

There is an exception to the acoustically defined spatial resolution limit discussed above. In the optical resolution microscopy mode of PA imaging (OR-PAM) described further in §4.2.2, a focused excitation laser beam is employed. For very small penetration depths (less than 1 mm), before the focused beam has been significantly distorted by optical scattering, the lateral spatial resolution is defined by the laser beam diameter at the focus. Under these circumstances, the lateral resolution is limited by optical diffraction which depends on the optical wavelength and the numerical aperture (NA) of the focusing lens and can be as small as few micrometres. Vertical resolution, however, remains limited by acoustic attenuation.

4. PHOTOACOUSTIC IMAGING CONFIGURATIONS

Photoacoustic imaging can be divided into several categories: PAT, PA microscopy and its variants. These categories are, to some extent, all variations on a theme and more a consequence of the different imaging instruments that have emerged in the last few years, than fundamental methodological differences.

4.1. Photoacoustic tomography

PAT can perhaps be regarded as the traditional mode of PA imaging as envisaged by early practitioners. It is also the most general and least restrictive PA imaging approach with the fewest limitations on imaging performance imposed by its practical implementation.

In PAT, full field illumination, in which a large diameter pulsed laser beam irradiates the tissue surface, is employed. At NIR wavelengths where tissue is relatively transparent, the light penetrates deeply and is also strongly scattered, resulting in a relatively large tissue volume becoming 'bathed' in diffuse light. Absorption of the incident radiation by tissue chromophores leads to impulsive heating of the irradiated tissue volume followed by the rapid generation of broadband ultrasonic waves. These propagate to the tissue surface where they are detected by a mechanically scanned ultrasound receiver or array of receivers. The time-varying detected ultrasound signals can then, with knowledge of the speed of sound, be spatially resolved and back-projected to reconstruct a three-dimensional image. Figure 2 shows three commonly used detection geometries: spherical, cylindrical and planar. Clearly, the

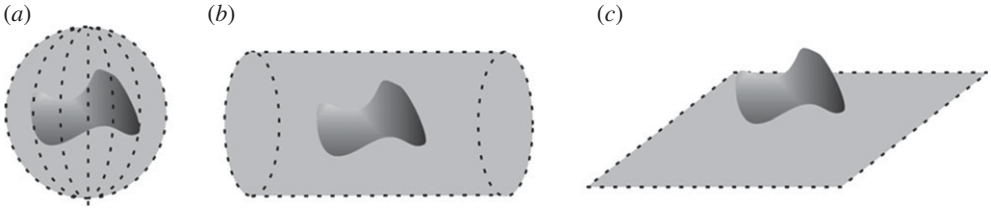

Figure 2. PAT detection geometries. (*a*) Spherical, (*b*) cylindrical and (*c*) planar.

cylindrical or spherical detection geometries requires access to all points around the target and are therefore limited to applications such as imaging the breast or small animals such as mice. Planar detection geometries are more versatile providing access to a greater range of anatomical targets, especially those superficially located.

A variety of methods for reconstructing the PAT image from the detected signals have been developed. Conceptually, the amplitude at each point t in the time record of the PA waveform recorded at a point r can be regarded as representing the sum of all points in the initial pressure distribution p_o that lie on a spherical surface centred on r and with a radius equal to the product of the sound speed and t—that is, to say the PA source distribution is regarded as being composed of an ensemble of elemental acoustic point sources each emitting spherical waves. The image reconstruction process can then be thought of as one in which each of the detected PA waveforms are spatially resolved using the sound speed, back-projected over spherical surfaces centred on r and summed over the image volume—figure 3 illustrates this for a planar detection geometry. This type of simple ad hoc back-projection is equivalent to delay-and-sum receive focusing or beamforming employed in phased array US imaging. Although it provides a simple and intuitively amenable description of PAT image formation and was used in early implementations [5,31], it is non-optimal in terms of accuracy and computational expense.

More advanced methods that provide a more accurate reconstruction and or greater computational efficiency have been developed in recent years, many of which are reviewed in Kuchment & Kunyansky [32,33]. These methods can be divided into several categories depending on the type of algorithm employed. Filtered backprojection-type algorithms involve filtering before or after a backprojection step [3] and can provide an exact reconstruction for spherical [34,35] cylindrical [36] and planar geometries [36]. Although computationally intensive, they have found practical application for spherical detection geometries used in PAT breast [27] and small-animal imaging [37]. A number of series summation-based methods, such as those based on the temporal and spatial spectral decomposition of the detected PA waveforms and a subsequent mapping to spatial frequency components in p_0 have been described [38,39]. They can provide an exact reconstruction for spherical [40], cylindrical [41], planar [42,43] and some other geometries such as a cube [39]. Only in the case of planar or cuboidal geometries can sufficiently fast computational times for practical

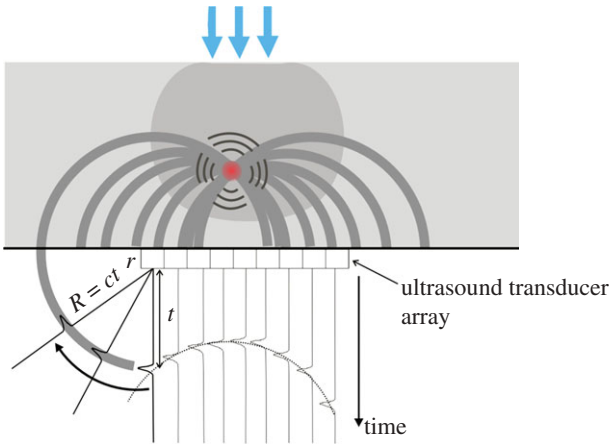

Figure 3. Backprojection PAT image reconstruction for a planar detection geometry. PA waveforms are recorded by each array element at r, spatially resolved using the sound speed c and backprojected over spherical surfaces of radius $R = ct$ into the image volume. Since the backprojected quantity is the velocity potential, the output of each detector is depicted as a time-integrated pressure waveform for illustrative purposes—in practice, the detectors record a pressure waveform and the time integration is performed computationally.

applications be achieved. In the more practically useful planar case, the implementation involves Fourier transforming the time-dependent pressure data measured over the surface, mapping the temporal frequency to the axial spatial frequency and inverse Fourier transforming to obtain p_0 [42]. It is computationally advantageous because much of the processing is accomplished via the fast Fourier transform and a simple k-space interpolation via the dispersion relation. This and its ease of computational implementation have led to its widespread practical use [29,44,45]. Time-reversal methods involve computationally re-emitting the measured PA waveforms at each detection point in temporally reversed order by running a numerical acoustic propagation model backwards [46–49]. They are perhaps the least restrictive of all algorithms [48], relying on the fewest assumptions and can be used for any detection geometry, detector distribution and can account for known acoustic heterogeneities. In addition, they can be used to mitigate for signal-to-noise ratio (SNR) and resolution degrading effects of acoustic absorption [49]. Although memory requirements are modest, for practical use, a fast numerical acoustic propagation model is required since it is necessary to compute the entire wavefield for each temporal backpropagation step. This has perhaps limited its practical application, although a time-reversal scheme

using an efficient pseudo-spectral k-space propagation model has been evaluated using experimental data [49,50]. Model-based inversion techniques employ a numerical forward model to simulate the detected PA signals from an initial estimate of p_0 or a related quantity [51,52]. An improved updated estimate can then be obtained by iteratively adjusting p_0 at each spatial point until the difference between the predicted and measured PA signals is minimized. By using matrix inversion methods and pre-computing for a specific geometry as described in Rosenthal *et al.* [53], these methods can be fast, albeit at the cost of flexibility and the significant computational expense of the initial pre-computing step.

Inevitably, there are practical limitations. An exact reconstruction usually requires the assumption of an infinite number of wideband omni-directional point-like detectors distributed over a solid angular detection aperture of 4π sr for a spherical[1] or cylindrical detection geometry and 2π sr for a planar geometry, the latter implying detection over an infinite plane—these aperture conditions mean that the entire acoustic wavefront is recorded, so there is a complete measured dataset. Adequately broadband piezoelectric ultrasound receivers that can provide the necessary megahertz bandwidth are, with some limitations, available. Achieving acoustically small detector element sizes in order to provide a near-omnidirectional response and a spatial sampling interval that fulfils the spatial Nyquist criterion ($<\lambda/2$) at megahertz frequencies is more challenging but possible, depending on the upper frequency limit. The detection aperture requirements can, however, present a more fundamental limitation. For spherical geometries, it is possible, in principle, to completely enclose the source region to fulfil the requirement of a 4π solid angular aperture. However, for cylindrical and planar geometries, the aperture is always truncated in practice. For planar detection geometries, in particular, measurements are always restricted to a finite region of the infinite plane that the reconstruction algorithm assumes. As a consequence, only part of the wavefront is recorded resulting in image artefacts and reduced spatial resolution—the so-called limited view or partial scan problem [54–56]. Artefacts, image distortion and blurring can also arise from sound speed heterogeneities and acoustic attenuation which are not accounted for in most reconstruction methods. Several methods aimed at compensating for sound speed perturbations [48,57] and acoustic attenuation [49] have been demonstrated with the aim of improving image quality in acoustically heterogeneous tissues.

Although most reconstruction methods rely on the assumption of detection by point-like omnidirectional receivers, there are techniques that employ mechanically scanned large-area directional planar detectors [58,59] or line detectors [60]. In the former case, the time-resolved output of the detector represents a set of time-retarded projections of p_0, over planes parallel to the detector rather than the projection of spherical surfaces that a point-like detector output represents. An image can then be reconstructed using the inverse radon transform analogous to that used in X-ray computed tomography (CT).

4.1.1. Photoacoustic tomography imaging systems. Spherical scanners: A variety of three-dimensional scanning instruments that employ a spherical detection geometry have been demonstrated. As noted above, for applications such as small-animal or breast imaging that allow the region of interest (ROI) to be enclosed by the detection surface, this geometry offers the highest practically achievable image fidelity on account of the large solid angular detection aperture that can be attained.

Figure 4 shows a spherical scanner design used for PA small-animal [37] and breast imaging [27]. The instrument comprises a hemispherical detector bowl with an aperture in the bottom to permit delivery of the excitation laser light. One hundred and twenty eight unfocused 5 MHz 3 mm-diameter piezoelectric elements are distributed in a spiral pattern over the surface. The bowl is mounted on a shaft to allow it to be incrementally rotated with successive excitation pulses so that sufficiently fine spatial sampling can be achieved. A second, smaller-diameter, optically and acoustically transparent bowl into which the breast is suspended is inserted inside the detector bowl. Both are filled with water to provide acoustic coupling. This arrangement allows the detector bowl to be rotated independently without disturbing the breast. The excitation light, sourced from a tunable optical parametric oscillator (OPO) laser system emitting at 800 nm and with a PRF of 10 Hz, is directed up through the aperture in the bottom of the bowl. A near-isotropic spatial resolution of approximately 250 μm over a 6.4 × 6.4 × 5 cm field of view (FOV) was reported. The image acquisition time obtained over this FOV using 240 angular steps per complete revolution was 24 s. Figure 4 shows a maximum intensity projection (MIP) images of the vasculature in the left breast of a patient volunteer with sub-millimetres vessels visible to a depth of 4 cm. The corresponding animated three-dimensional MIP movies available online (see electronic supplementary material, movies S1 and S2) perhaps best illustrate the full extent of the detailed vascular anatomy revealed by these images. The *in vivo* penetration depth achieved in this study provides a compelling demonstration of the deep tissue imaging capability of PAT, especially as the optical fluence used was more than one order of magnitude lower than the safe maximum permitted exposure (MPE) for skin.

A spherical detection geometry can also be achieved by arranging the detectors over an arc and then axially rotating the target located within the interior space to synthesize detection over a spherical surface as described in Kruger *et al.* [61]. In this study, *ex vivo* images of a mouse were obtained. Another small-animal scanner that uses a similar approach has been described in Brecht *et al.* [62] and was used to acquire

[1]There are some exceptions to this for a spherical geometry. For example, an exact reconstruction of an object that lies within a hemispherical detection surface (ie 2π sr) can be obtained.

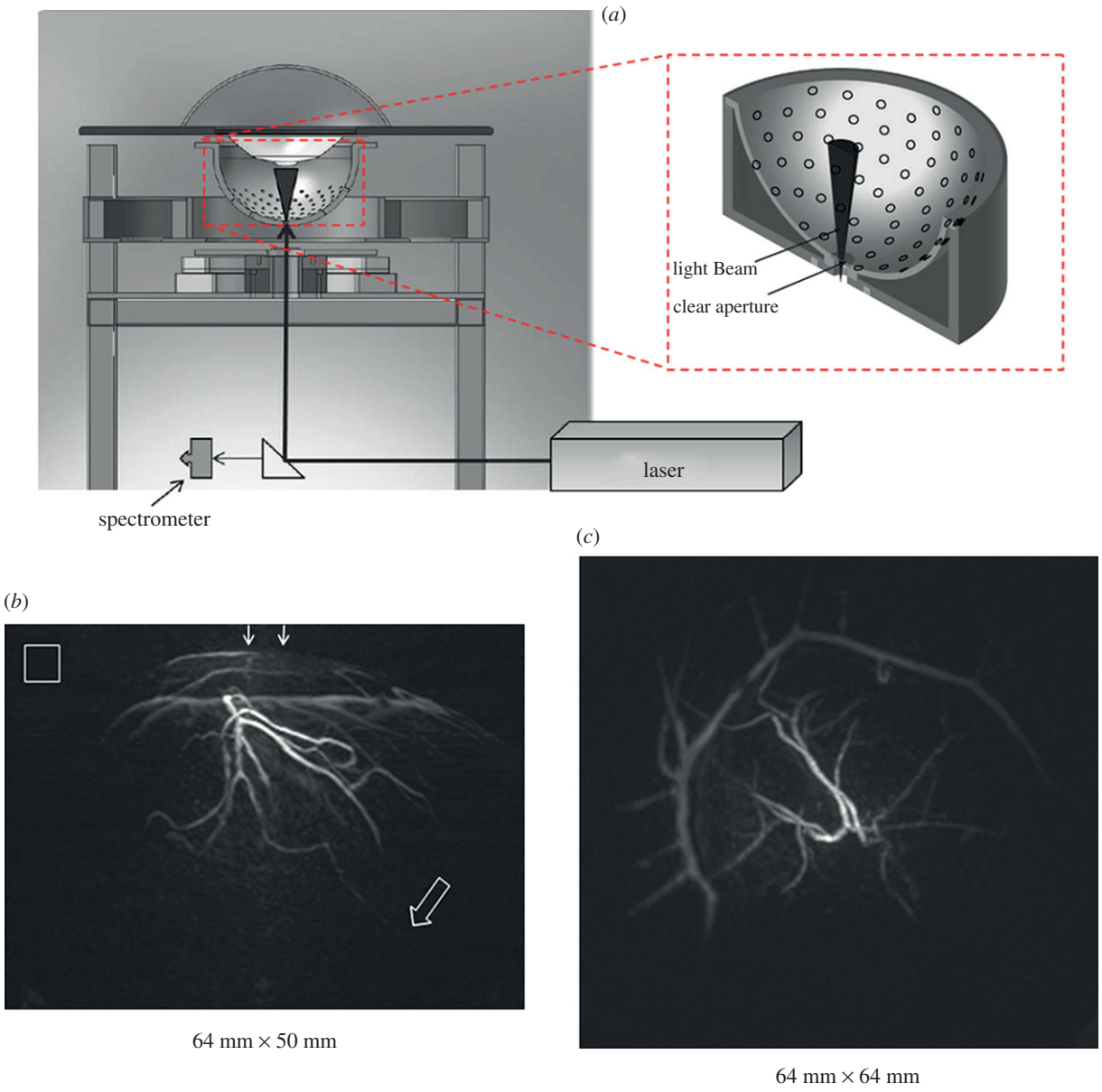

Figure 4. PAT breast scanner with hemispherical detection geometry [27]. (*a*) Schematic of system. (*b*) MIP of the left breast of patient volunteer (lateral projection) over 64 × 50 mm^2 FOV. Arrows at top indicate the direction of the incident excitation light. Hollow arrow marks the position of a vessel at a depth of 40 mm. Hollow box represents 1 × 1 cm^2 (*c*) orthogonal (anterior–posterior) projection 64 × 64 mm^2 FOV. Excitation laser wavelength: 800 nm. Three-dimensional animated MIP movies of both projections can be viewed online at the electronic supplementary material, movies S1 and S2.

in vivo whole-body images (figure 5). In this scheme, the arc array comprised 64 square (2 × 2 mm) piezocomposite transducers of centre frequency 3.1 MHz distributed over a two-dimensional angular aperture of 152°. When the object is rotated through 360°, this translates to a solid angular detection aperture of 10.6 sr and thus close to the ideal 4π sr aperture required for an exact reconstruction. The animal is immersed in water, with a diving bell arrangement to allow for the delivery of anaesthetic and respiratory gases and placed at the centre of the array as depicted in figure 5. Fibres placed orthogonal to the plane of the array and directed at the mouse provide 755 nm excitation pulses emitted by an Alexandrite laser with an incident surface fluence of 1 mJ cm^{-2}. To preferentially emphasize the PA waves emitted by anatomical features of different length scales and geometries, the raw RF-detected signals were processed with a family of wavelet and other filters prior to image reconstruction, the latter being achieved using a spherical backprojection algorithm. The spatial resolution was reported to be 0.5 mm and the acquisition time was 8 min based on 150 steps per complete revolution of the animal and averaging over 32 laser pulses. Figure 5 shows a volume-rendered image obtained by the system demonstrating that internal organs, such as the spleen, liver and kidney can be visualised. The benefits of incorporating prior structural information into the formation of the image, in this case via the wavelet filtering referred to above, in order to selectively enhance organs, blood vessels and other anatomical structures are apparent.

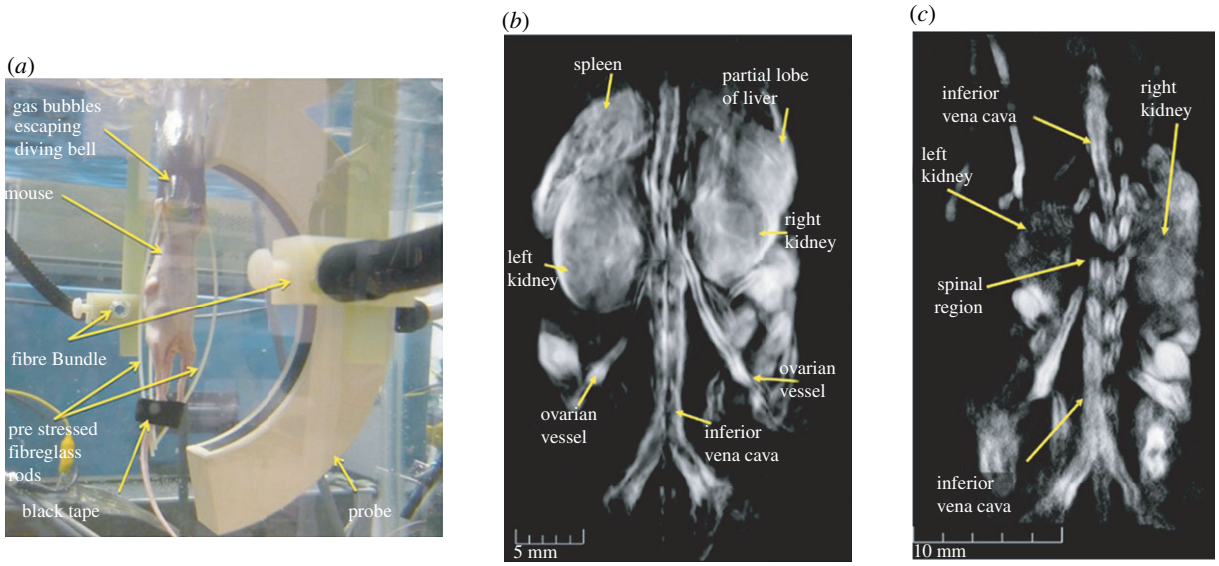

Figure 5. PAT whole body small animal scanner based on a spherical detection geometry [62]. (*a*) Experimental arrangement showing 64 element arc array and fibre delivery bundle. (*b*) Three-dimensional image of a nude mouse illuminated at 755 nm. Both kidneys are visualized as well as the spleen and a partial lobe of the liver. (*c*) Image showing spinal region and left and right kidneys. Three-dimensional-animated movies of the two images can be viewed online at electronic supplementary material, movies S3–S5.

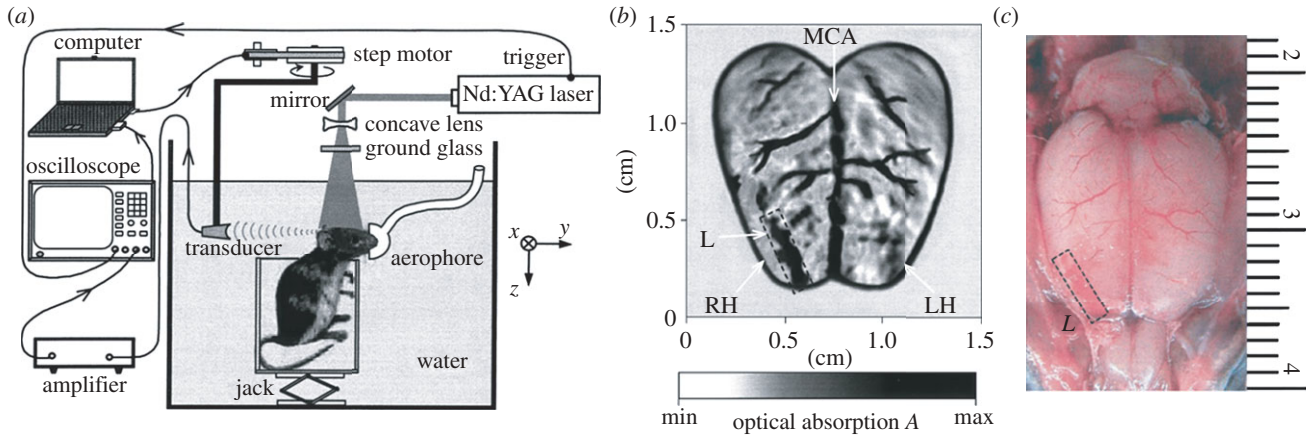

Figure 6. PAT cylindrical scanner for small animal brain imaging [64] (*a*) experimental arrangement. (*b*) Image showing superficial cortical vasculature and a surgically induced lesion. MCA: middle cerebral artery, RH: right cerebral hemisphere, LH: left cerebral hemisphere. (*c*) Photograph of cerebral surface following resection of the skull after PAT image acquisition. Laser wavelength: 532 nm.

Cylindrical scanners: Although a true two-dimensional cylindrical detection geometry has rarely been implemented for three-dimensional imaging in practice ([63] being an exception), its one-dimensional equivalent, recording over a circle or an arc to obtain a two-dimensional cross-sectional image, has been widely implemented. Its popularity stems from its ease of implementation and the ability to acquire a high-fidelity image with few artefacts—a consequence of the fact that detection over a full 360° angular aperture can readily be achieved for targets that can be enclosed. If high frame rates are not required, it can also be inexpensively implemented as a laboratory system using a single mechanically scanned receiver and a stepper motor-driven rotational stage. Although widely used, it is, in common with the spherical detection geometry, inevitably limited to applications such as small-animal [64–73] or breast [74,75] imaging.

Figure 6 shows perhaps the simplest one-dimensional cylindrical scanner for two-dimensional cross-sectional imaging [64]. It comprises a single 3.5 MHz PZT transducer, focused in the elevation direction to attenuate out-of-plane signals, that is mechanically scanned around the target, in this case the mouse head. The excitation laser light (at 532 nm) is delivered along the axis of rotation in order to transversely irradiate the surface. Although the attenuation of light at 532 nm in tissues is relatively high, as figure 6 shows, the superficial cortical vasculature can still be visualized with high contrast. The spatial resolution of the system

was estimated at approximately 200 μm. Following this early demonstration, a variety of similar single-element mechanically scanned laboratory systems have been used variously to image epileptic events [65], tumour growth [67] and cerebrovascular changes [66] in mice and peripheral joints [76]. To overcome the long image acquisition times of these systems (minutes to hours), several array-based cylindrical scanners that provide real-time two-dimensional image frame rates have been developed and used to study cerebral haemodynamics [70–72], cardiovascular dynamics [69] and organ perfusion [68] in mice. One of these systems employs a 512-element array arranged over a full 360° aperture [70]. With 8 : 1 multiplexing, a single acquisition of all elements could be achieved in 1 s. This permitted dynamic imaging of the wash-in of a systemically introduced contrast agent as it perfused through the superficial cortical vasculature in a mouse. A similar system but employing 64 elements over the arc of a 180° aperture has been used for whole-body small-animal imaging [68,69]. Three-dimensional images were obtained by axially translating the target in the *z*-direction and concatenating the two-dimensional cross-sectional slices acquired at each axial step. This system was used to acquire structural images of the abdominal, thoracic and heart regions. Its high image frame rate (10 Hz) enabled dynamic events such as motion of the heart chambers and ICG-mediated kidney perfusion to be visualized in real time. Another approach employed a fixed 128-element linear ultrasound array and a rotating target holder to implement a two-dimensional cylindrical detection scheme [77]. This system was used to obtain *ex vivo* PA images of the mouse upper body and both PA and US images of phantoms.

Planar scanners: Although spherical and cylindrical detection geometries can provide the large angular aperture required for an accurate image reconstruction, their applicability is constrained by the need for access to all sides of the target. They are not suitable for imaging highly superficial features, such as the skin microvasculature, or if strongly echogenic structures such as bone or lung are situated along the acoustic propagation path. These circumstances call for the more versatile planar detection geometry in which the detection is performed over a finite plane using a two-dimensional ultrasound array or its one-dimensional equivalent, detection over a line using a linear array. PA imaging instruments that employ this geometry begin to resemble conventional diagnostic clinical US scanners, in some cases comprising a hand-held array probe that is acoustically coupled to the skin and moved around while viewing the images in real time. Indeed, a variety of PA imaging instruments use existing commercially available diagnostic scanners, suitably modified so that the RF acquisition can be triggered by the excitation laser in order to detect PA waves as well as US echoes [44,77–80]. Co-registered PA and US images can then be reconstructed either using the hardware beamformer of the scanner or in a post-processing step using a reconstruction algorithm. Thus, the absorption-based contrast provided by the PA image can be exploited to reveal the structure and function of the vasculature while the US image provides information on the surrounding tissue morphology based on its elasto-mechanical properties. In this way, the different but complementary contrast provided by each modality can be used in combination to provide additional diagnostic information.

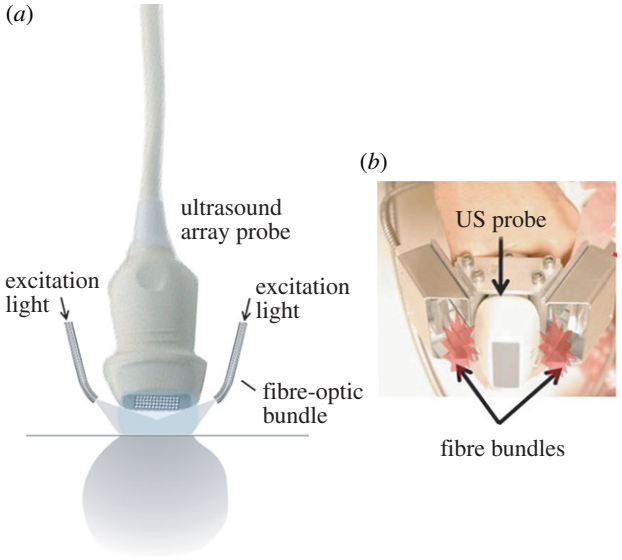

Figure 7. Use of a conventional ultrasound imaging probe for PA imaging. (*a*) Two-dimensional array probe. (*b*) Implementation using a linear array probe for dual mode PAT-US imaging described in Kim *et al.* [29].

Although more versatile, particularly for clinical use, image quality provided by a planar detection geometry rarely matches that image quality provided by spherical and cylindrical geometries because of the limited detection aperture. As well as introducing artefacts and distortion, this also reduces lateral spatial resolution—indeed, it is the limited view, not frequency-dependent acoustic attenuation, that tends to limit lateral resolution. Vertical resolution, on the other hand, is relatively independent of the detection aperture and is limited by acoustic attenuation. This results in a disparity between the lateral and vertical resolution and gives rise to an anisotropic spatial point spread function, itself a source of image distortion. Delivering the excitation laser light can also be problematic if an array of receivers rather than a single mechanically scanned receiver is employed. The usual solution is to vertically offset the array from the tissue surface, fill the intervening space with an optically transparent acoustic couplant and deliver the laser light obliquely to the tissue surface beneath the array as illustrated in figure 7*a*. This is readily achievable if a linear array is used for two-dimensional imaging as the excitation laser beams can be delivered orthogonal to the length axis of the array and so only have to 'clear' the width of the transducer elements. However, the requirement for a spacer does impose a limitation on the dimensions of a two-dimensional array that can be used—the larger the area, the greater the required spacer thickness which in turn reduces the effective detection aperture and thus image quality.

Figure 7*b* shows a specific implementation in which a commercially available diagnostic linear array probe

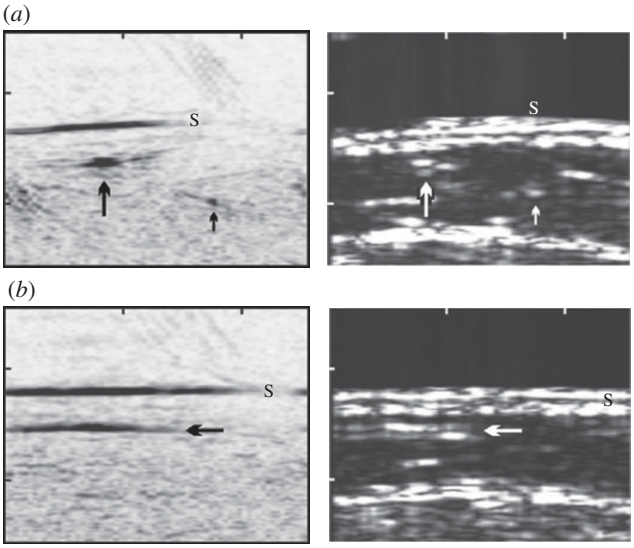

Figure 8. (left) *In vivo* PAT images and (right) corresponding US images of a vein at the interior part of the medial lower leg obtained using a linear ultrasound array [44]. The image area is 2.6×2 cm (ticks every centimetre) (*a*) Cross-sectional image from the interior part of the leg. In the PAT image (left), the skin (S) is visible as a black line. Black and white arrows identify the location of common blood vessels observed in both PAT and US images (*b*) Images acquired at the same location but in the orthogonal plane. Laser wavelength: 760 nm.

and a pair of fibre bundles are integrated to form a hand-held dual-mode US-PA imaging head [29]. This system provides co-registered two-dimensional PA and US images at real-time image frame rate (10 fps) and is intended for a relatively deep tissue imaging application: sentinel lymph node detection in the breast. Other similar schemes have been demonstrated for visualizing superficial vascular anatomy, including one that employs a 64-element, 7.5 MHz linear array that also provides real-time laser PRF-limited frame rates (7.5 fps) [44]. An example of a PA and US image provided by this system is provided in figure 8 showing the blood vessels at a depth of around 10 mm in the leg. Fronheiser *et al.* [79] describe the use of a dual PA–US system that uses a 128-element linear array probe from a commercial ultrasound scanner to image the vasculature in the arm in real time with a view to identifying vessels prior to haemodialysis. A 1.75 D phased array comprising 1280 elements has also been used to provide three-dimensional co-registered PA and US images [80]. The Visualsonics small-animal ultrasound scanner has also been adapted to provide a dual-mode PA–US imaging capability in an instrument that is now commercially available [81].

The use of existing, commercially available ultrasound scanners is a convenient and relatively inexpensive means of implementing PA imaging that exploits the advances in piezoelectric array technology, hardware beamformers and RF acquisition electronics that have taken place in recent years in diagnostic ultrasound imaging. However, PA image quality obtained using these systems tends to be somewhat limited, particularly for superficial imaging applications. This is in part a consequence of the limited detection aperture that linear array-based systems provide. It is also because the transducers used in clinical US scanners tend to operate in the sub-10 MHz range and are resonant to some degree. They are, therefore, often insufficiently broadbanded for the detection of PA waves emitted by superficial structures, the frequency content of which can extend from the low megahertz to several tens of megahertz. To address this a custom designed high-frequency 48-element linear array fabricated from 2–2 piezocomposite elements with a centre frequency of 30 MHz and a 70 per cent fractional bandwidth has been developed for PA imaging [82,83]. As with other linear arrays used for PA imaging, it provides a real-time two-dimensional B-scan frame rate, in this case 50 fps. By rapid mechanical scanning, a volumetric frame rate of 1 fps for 166 B-scans was reported and the system used to image the subcutaneous vasculature in the human and rat.

A different approach, based on an optical method of ultrasound detection, has been explored with a view to overcoming the limitations of piezoelectric-based detection for planar geometries. It employs a transparent Fabry–Perot (FP) polymer film etalon that comprises a polymer film spacer sandwiched between a pair of mirrors [84,85]. Acoustically induced changes in the optical thickness of the spacer modulate the reflectivity of the etalon which can be detected by measuring the changes in the reflected power of an incident laser beam. By raster scanning a focused laser beam across the surface of the sensor, an incident PA wavefront can therefore be spatially mapped in 2D (figure 9*a*). There are several advantages of this concept. First, the mirrors of the etalon can be designed to be transparent to the excitation laser wavelength. The sensor head can therefore be placed directly on the surface of the skin, and the laser pulses transmitted through it into the underlying tissue. It thus avoids the detection aperture limitations imposed by an acoustic spacer required for piezoelectric detection methods. It also provides an inherently broadband response from DC to several tens of megahertz and very fine spatial sampling of the incident acoustic field. The effective acoustic element size is defined, to a first approximation, by the diffraction limited dimensions of the focused interrogation laser beam. The notional element size and interelement spacing can therefore be on a scale of tens of micrometres. Perhaps, most importantly, the small element size is achieved with significantly higher detection sensitivity that can be provided by similarly broadbanded piezoelectric receivers of the same element dimensions [85]. The combination of a transparent sensor head and wideband acoustic performance attributes makes this type of sensor particularly well suited to imaging superficial features located within a few millimetres of the tissue surface. In these circumstances, the short acoustic propagation distances involved mean that the PA signal is only weakly bandlimited by acoustic attenuation and can therefore be extremely broadbanded with a frequency content extending to several tens of megahertz. The requirement for a broadband omnidirectional point detector for an accurate image reconstruction then becomes particularly challenging

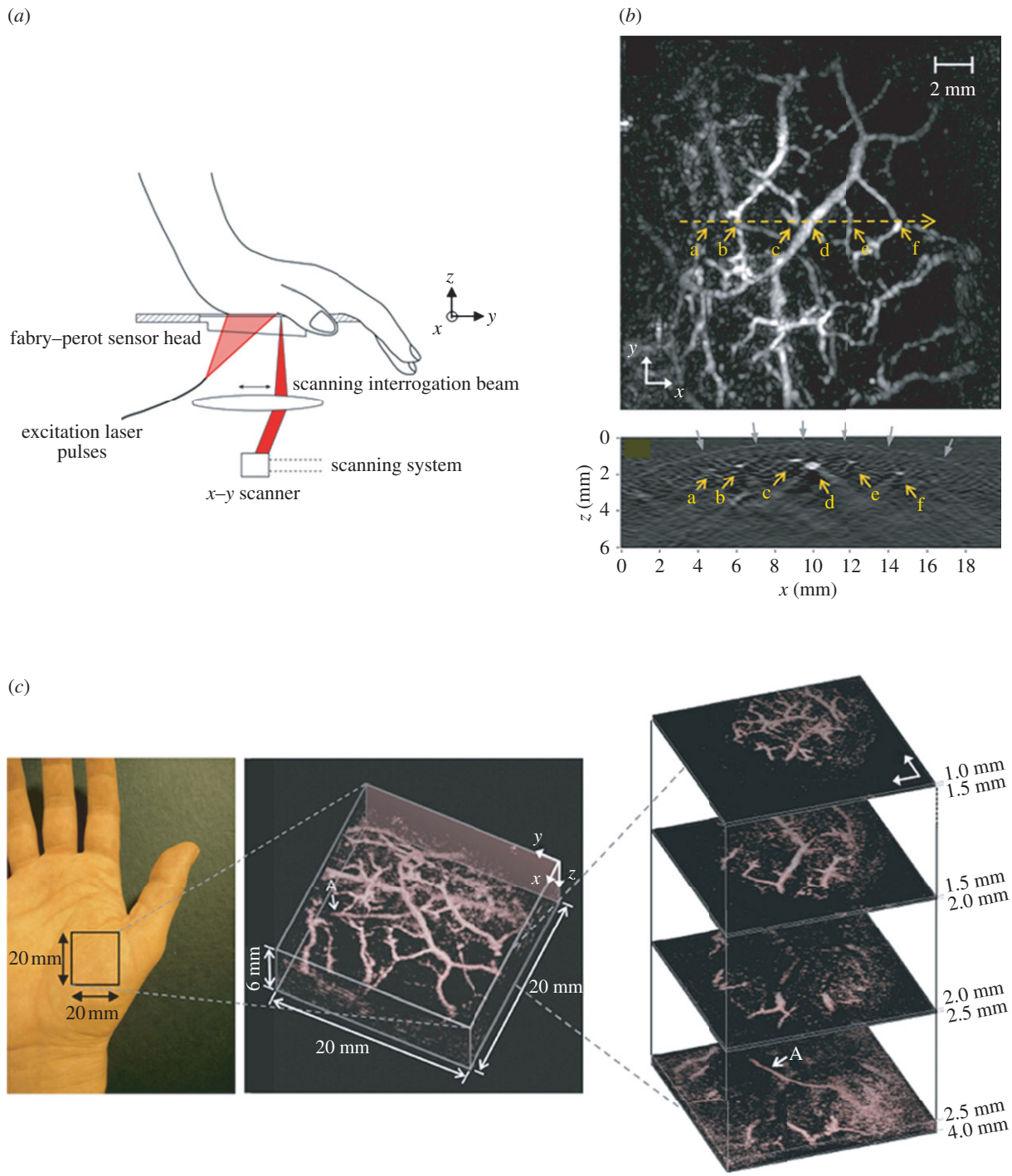

Figure 9. (*a*) Schematic of FP-based photoacoustic scanner used to acquire a three-dimensional image of the vasculature in the palm [45]. (*b*) Lateral MIP image (top) and vertical (x–z) slice image (bottom) taken along horizontal yellow dotted line on MIP. Grey arrows indicate the contour of the skin surface. (*c*) Left: photograph of the imaged region, middle: volume rendered image. An animated representation of this image can be viewed online at electronic supplementary material, movie S6, and right: lateral slices at different depths. The arrow 'A' indicates the deepest visible vessel, which is located 4 mm beneath the surface of the skin. Laser excitation wavelength: 670 nm.

using conventional piezoelectric detection as it demands element dimensions of a few tens of micrometres. Fabricating piezoelectric elements of such small size with adequate detection sensitivity is problematic since their sensitivity scales with active area. By contrast, the FP sensor sensitivity is, to a first approximation, independent of element size.

A schematic of the system is shown in figure 9*a* along with several representations of the three-dimensional image dataset obtained by scanning the human palm [45]. The sensor used for this demonstration had a peak noise-equivalent-pressure (NEP) of 0.2 kPa (over a measurement bandwidth of 20 MHz) and a −3 dB detection bandwidth from 100 kHz to 22 MHz. The interrogation laser beam spot size was 64 μm, spatial sampling interval was 250 μm and an FOV was 20 mm. No signal averaging was used. The excitation wavelength was 670 nm and the incident fluence

incident on the skin surface was 10 mJ cm^{-2}, and thus below the MPE of 20 mJ cm^{-2} for skin at this wavelength [86]. Figure 9*b* shows a lateral MIP and a single vertical slice through the centre of the lateral MIP as indicated. This vertical slice shows the contour of the skin surface as well as several underlying subdermal blood vessels. Figure 9*c* shows a volume-rendered representation of the reconstructed image and a series of lateral slices at different depths. These images show the subcutaneous vasculature to a depth of approximately 4 mm—the deepest lying vessel is indicated by the arrow 'A' on both the volume-rendered image and the deepest lateral slice. The time taken to acquire the three-dimensional image data shown in figure 9 was approximately 10 min, limited by the sequential nature of the detection and the low PRF of the excitation laser (10 Hz). There is, however, scope to increase acquisition speed, potentially obtaining real-time three-dimensional image acquisition rates, through the use of higher repetition rate laser systems or parallelizing the sensor read-out scheme using full-field illumination and a photodetector array as described in Lamont & Beard [87]. As well as imaging the skin vasculature, the system has been used for imaging tumour vasculature [45,88], the mouse brain [89] and embryo [50,90].

4.2. Photoacoustic microscopy

PA microscopy refers to techniques in which a PA image is obtained by mechanically scanning either a focused ultrasound detector or a focused laser beam. The image is then formed directly from the set of acquired A-lines, without the aid of a reconstruction algorithm as in PAT. If a focused ultrasound detector is used, it is termed acoustic resolution PA microscopy (AR-PAM) since axial and lateral spatial resolution is defined by the physics of ultrasound propagation and detection. If a focused laser beam is used, it is termed OR-PAM since the spatial resolution in at least one plane (usually, the lateral) is defined by the spatial characteristics of a focused laser beam propagating in tissue. Despite the name, PA microscopy, unlike its optical equivalent, does not necessarily imply the observation of anatomy on a small length scale—AR-PAM, for example, can be used to image to depths of several centimetres.

4.2.1. 'Acoustic resolution' photoacoustic microscopy. The term AR-PAM is usually used to describe implementations that employ a single mechanically translated or rotated focused transducer to map the PA signals [91–100]. Figure 10 shows one approach that has been extensively used. It comprises a focused receiver around which the excitation light is delivered, usually using a conical lens that produces a hollow cone of weakly focused light within which the transducer is placed. Optical focusing is not essential as it does not serve to localize the signal and thus does not influence the spatial resolution. Full-field illumination could equally be used as in PAT but confining the excitation beam by weakly focusing it reduces the laser energy requirements. It also reduces the large PA signal generated at the surface. This can otherwise obscure later arriving signals owing to ringing if a resonant transducer such as one fabricated from PZT is used. To acquire a 3D image, both the transducer and the excitation beam are mechanically scanned together over a planar surface, generating and detecting PA waves at each step of the scan. The resulting two-dimensional sequence of detected acoustic signals or A-lines, each of which represents a depth profile of absorbed energy, is then rectified, envelope detected, spatially resolved and mapped to a greyscale to form a three-dimensional image directly. Unlike PAT, an explicit reconstruction algorithm is not employed although this is more a difference in implementation than physical principle—if PAT image reconstruction is regarded as *in silico* point-by-point receive beam forming, then it is apparent that the focused receiver itself performs this function for each x–y scan position. Figure 10 shows an image of the skin vasculature in the forearm region obtained using AR-PAM illustrating the dermal and sub-dermal vasculature. The system was also used to image a benign-pigmented skin lesion to demonstrate the potential for identifying melanomas via their morphology and composition. The transducer frequency was 50 MHz, the fractional bandwidth 70 per cent, the aperture 5.8 mm, depth of focus 0.3 mm and focal length 6.7 mm giving a lateral resolution at the focus of 45 μm and a vertical resolution of 15 μm. For an 8×8 mm FOV and a step size of 20 μm, the acquisition time was approximately 5 min. Similar high-resolution AR-PAM systems have been used in preclinical studies of the mouse brain [96] and skin microvasculature [101]. The length scale that AR-PAM can address is scalable. By reducing the transducer bandwidth and increasing the focal length, it has been used to visualize organs at depths of several centimetres in the mouse, albeit with a reduced spatial resolution of a few hundred micrometres [95,96].

As figures 4–6,9 and 10 show, both AR-PAM and PAT can provide compelling images over a range of spatial scales. However, there are significant differences between the two techniques in terms of performance, cost and complexity. An important difference relates to the factors that affect spatial resolution over the FOV. For a planar detection geometry, the lateral spatial resolution of PAT at a specific point in the illuminated volume is ultimately defined by frequency-dependent acoustic attenuation and the solid angle subtended by the detection aperture to that point. Thus at all points in the three-dimensional FOV, the lateral resolution can be said to be acoustic diffraction-limited which represents the fundamental resolution limit. However, in AR-PAM, this is only so at the depth corresponding to the location of the transducer focus. Elsewhere, the lateral resolution degrades rapidly. To obtain true acoustic diffraction-limited resolution over the entire three-dimensional FOV necessitates axial as well as lateral mechanical scanning with a consequent increase in acquisition time. The problem can be ameliorated to some extent using synthetic aperture focusing [102]. Another possibility that has been explored is the use of an axicon reciever [103]. Based on the theory of non-diffracting acoustic Bessel beams,

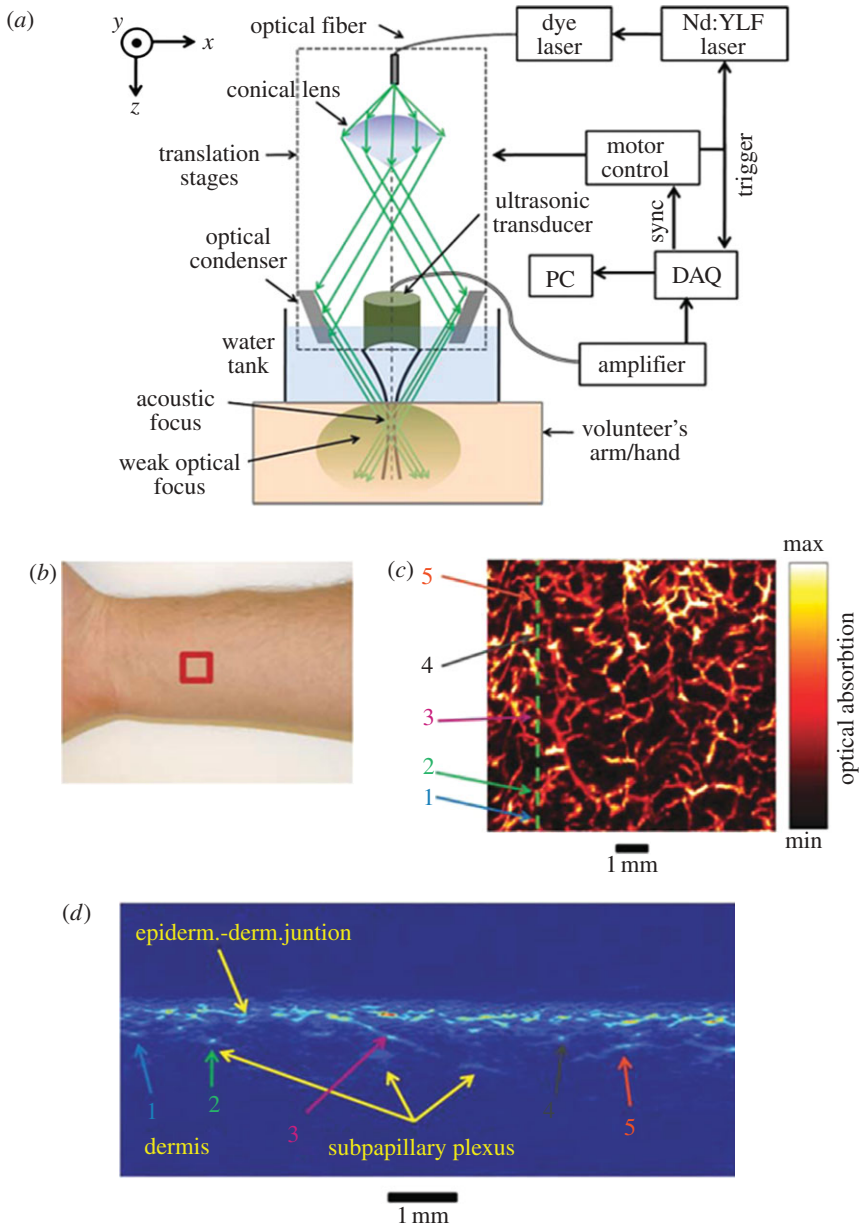

Figure 10. Acoustic-resolution photoacoustic microscopy (AR-PAM) system used for imaging the skin vasculature [94]. (*a*) Schematic of system, (*b*) region of forearm scanned, (*c*) lateral x–y MIP image (FOV = 8 × 8 mm), (*d*) vertical x–z slice image taken along vertical line in (*c*). Laser excitation wavelength: 584 nm.

this can, in principle, provide a non-divergent receive focus that could potentially eliminate the need for depth scanning.

A further distinction between PAT and AR-PAM lies in the complexity and cost of implementation. The laser power requirements for AR-PAM are more modest than those of PAT. In PAT, the entire three-dimensional FOV must be irradiated whereas in AR-PAM only the region that coincides with the receive beam profile of the transducer is required to be illuminated for each scan position. By confining the internal light distribution to this region by weak focusing, a laser pulse energy that is an order of magnitude lower than that required for PAT can be used. This allows a greater variety of laser sources to be used, particularly those that offer higher PRFs and a tunable output. AR-PAM can also be straightforwardly and inexpensively implemented as a laboratory-based research tool using a single mechanically scanned receiver. However, there is little scope to parallelize the detection using an array to overcome the limitations on acquisition speed imposed by mechanical scanning. PAT detection, on the other hand, can readily, if expensively, be parallellized using an array of receivers and, in principle, provide real-time three-dimensional image frame acquisition. For high-resolution superficial imaging to depths of few millimetres, AR-PAM has the advantage that, unlike PAT, it does not require acoustically small receivers on a tens of micrometre scale. As discussed in §4.1.1, these are difficult to fabricate with adequate detection sensitivity using piezoelectric receivers although the optical etalon detectors described in the previous section may provide a solution to this. In summary, PAT offers the ultimate imaging

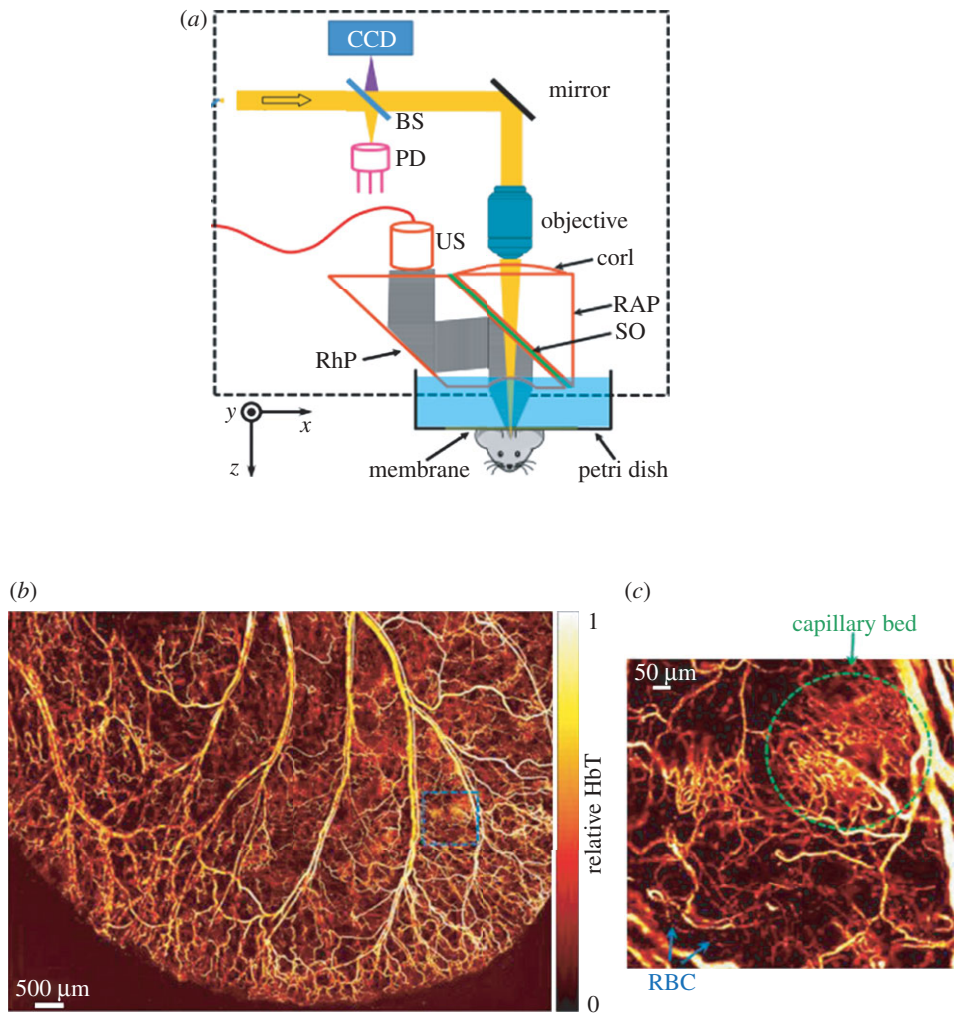

Figure 11. Optical-resolution photoacoustic microscopy (OR-PAM) scanner used for *in vivo* imaging of the mouse ear [118]. (*a*) Schematic of system BS, beam splitter; PD, photodiode; CorL, correction lens; RAP, right-angle prism; SO, silicone oil; RhP, rhomboid prism; US, ultrasonic transducer (50 MHz). The CCD is used to view the imaging region. The components that lie within the dotted rectangle form the scan head, which is mechanically translated in order to acquire an image. (*b*) *In vivo* image of the microvasculature in the mouse ear. (*c*) Expanded region shows capillary network and red blood cells (RBC) within a capillary. Excitation wavelength: 570 nm.

performance in terms of spatial resolution and acquisition speed, but in its most sophisticated form is considerably more complex and expensive than AR-PAM.

4.2.2. 'Optical resolution' photoacoustic microscopy. A second mode of PA microscopy is the so-called 'optical-resolution' mode (OR-PAM) in which optical rather than acoustic confinement is exploited for localization [99,104–118] purposes. It is in many ways more akin to optical microscopy than acoustic imaging in that lateral resolution is defined by the dimensions of a tightly focused diffraction-limited laser beam which is used to generate the PA waves. Also in common with optical microscopy, it is a strictly superficial imaging technique with a maximum penetration depth of approximately 1 mm in most tissues due to optical scattering. However, an important distinguishing feature is that unlike any of the current variants of optical microscopy, it provides optical absorption-based image contrast.

Figure 11 shows a schematic of one implementation. A high numerical aperture (NA) optical lens is used to focus the excitation laser beam onto the tissue surface and an optically transparent acoustic reflector directs the PA wave to an ultrasound transducer. By mechanically scanning the focused excitation beam and the transducer together and recording the detected A-lines at each point, a three-dimensional image can be formed as in AR-PAM. However, unlike AR-PAM, lateral resolution for depths less than approximately 1 mm (beyond this optical scattering defocuses the beam and degrades resolution) is defined by the diffraction-limited dimensions of the focused laser beam. Compared with AR-PAM, much higher lateral resolution of the order of a few microns can therefore be achieved over this depth range. To achieve a comparable acoustic diffraction-limited resolution with AR-PAM would require a broadband acoustic frequency content extending to several hundred MHz. Although it is possible to generate PA waves with such a broad bandwidth, acoustic attenuation at such high frequencies is much higher than optical

attenuation and would limit penetration depth to approximately 100 μm [105]. By contrast, in OR-PAM, the maximum penetration depth of approximately 1 mm is a consequence not of optical or acoustic attenuation but the spreading and distortion of the excitation laser beam owing to tissue optical scattering which prevents a tight focus from being maintained beyond this depth.

The high lateral resolution available to OR-PAM enables *en face* images of individual capillaries [105] and even individual red blood cells (RBCs) to be visualized in the mouse ear as shown in figure 11 [118]. Although these images illustrate the very high optically defined lateral resolution of OR-PAM, vertical resolution is about one of magnitude lower (typically approx. 10 μm) as it depends on acoustic propagation and detection and is thus limited by acoustic attenuation or the detector bandwidth as in AR-PAM or PAT. The disparity in lateral and vertical resolution can be ameliorated in part using nonlinear optical excitation methods which provide optically defined axial as well as lateral spatial localization. However, these techniques require three-dimensional scanning to provide a volumetric image [112]. Indeed, even in conventional OR-PAM, a degree of axial scanning is required for three-dimensional imaging as the highest lateral resolution occurs only at the depth of the optical focus. In addition to the configuration shown in figure 11, several other implementations have been reported. Xie *et al.* [107] describe an alternative scanning method that was also used to image blood vessels in the mouse ear [119] and subsequently the retina [121]. This approach avoids the frame rate limitations of mechanically scanned methods by optically scanning a focused PA excitation beam across the tissue surface using an x–y galvanometer scanner and detecting the PA signals with a single stationary planar ultrasound receiver offset from the scan area. Although higher frame rates are attainable with this method, they are achieved at the cost of a reduced FOV, limited by the directional response of the receiver. A further development in OR-PAM involves the use of adaptive optics. To date this has been used to correct for aberrations in the scan lens and light delivery optics [114] but could also potentially be employed to compensate for optical wavefront distortion in tissues to extend penetration depth. The optical detection system described in §4.1.1 has also been used to perform both PAT and OR-PAM enabling the different spatial scales of each modality to be addressed with the same instrument [113].

Although *in vivo* OR-PAM is very much a superficial imaging technique, limited mainly to imaging the mouse ear and brain (with the skin removed), it provides a useful adjunct to the current armoury of PA imaging techniques. A key attribute is that PA Doppler flowmetry (§5.2) and the spectroscopic measurement of blood oxygenation (§5.1) are significantly less challenging to implement using OR-PAM than PAT and AR-PAM. These functional capabilities make OR-PAM a powerful research tool for basic preclinical investigations of oxygen supply and delivery at capillary level. With the exception of opthalmic applications [119,121] clinical applications of OR-PAM are inevitably limited owing to the short penetration depth it provides.

4.3. Endoscopic devices

There are several potential clinical applications in which the target tissue can only be accessed by introducing a miniature endoscopic probe percutaneously or through a natural orifice. Among these are the clinical assessment of coronary artery disease, prostate cancer and gastrointestinal pathologies. A number of prototype PA endoscopic or intravascular devices, conceptually similar to conventional US probes, have been developed [122–130] for these applications. Intravascular PA imaging employs a sideways looking rotating probe in a manner analogous to IVUS. Figure 12 shows one such configuration [127]. It comprises a 1 mm diameter 30 MHz PZT transducer located at the end of a catheter in close proximity to the tip of an angle polished optical fibre that delivers the PA excitation laser pulses. The total outer diameter of the assembly is 1.25 mm and thus of comparable dimensions to those required for intravascular imaging in human coronary arteries. As well as providing cross-sectional PA images by rotating the catheter and acquiring PA A-lines at each angular step, the transducer was operated in pulse-echo mode enabling a co-registered IVUS image to be acquired simultaneously. Figure 12 shows PA and US images obtained *ex vivo* in human coronary arteries. In order to identify lipid-rich regions, the PA images were obtained at the peak lipid absorption wavelength of 1210 nm and, for comparison, at 1230 nm where absorption is low [131,132]. A variety of other PA intravascular probe designs based on different light delivery and ultrasound detection mechanisms have also been demonstrated [123,125,128]. As yet, none has been evaluated *in vivo*. This is in part due to the technical challenges involved in integrating the delivery optical fibre with a conventional piezoelectric detector while achieving the necessary level of miniaturization for intravascular use. The use of the optical ultrasound detector referred to in §4.1.1 may be able to address this. A 250 μm diameter sideways looking PA imaging probe based on this type of sensor, the smallest PA probe developed to date, has been described [128]. Other miniature probe designs have been proposed or evaluated for other applications. One of these employs a commercial 128-element forward-looking endocavity ultrasound probe to detect the PA waves and has been proposed for prostate imaging [124] applications. Yang *et al.* [122] describe a sideviewing dual-mode PA and US imaging probe. This uses a rotating 45° optical and acoustic mirror located at the tip of the device to deliver the excitation light and receive the PA signal thereby avoiding the need to rotate the catheter shaft. The diameter of the probe is relatively large at 4 mm although sufficiently small for gastrointestinal use.

5. PHOTOACOUSTIC SENSING TECHNIQUES

5.1. Photoacoustic spectroscopy

A major advantage of PA imaging is that image contrast can be selectively enhanced for specific tissue

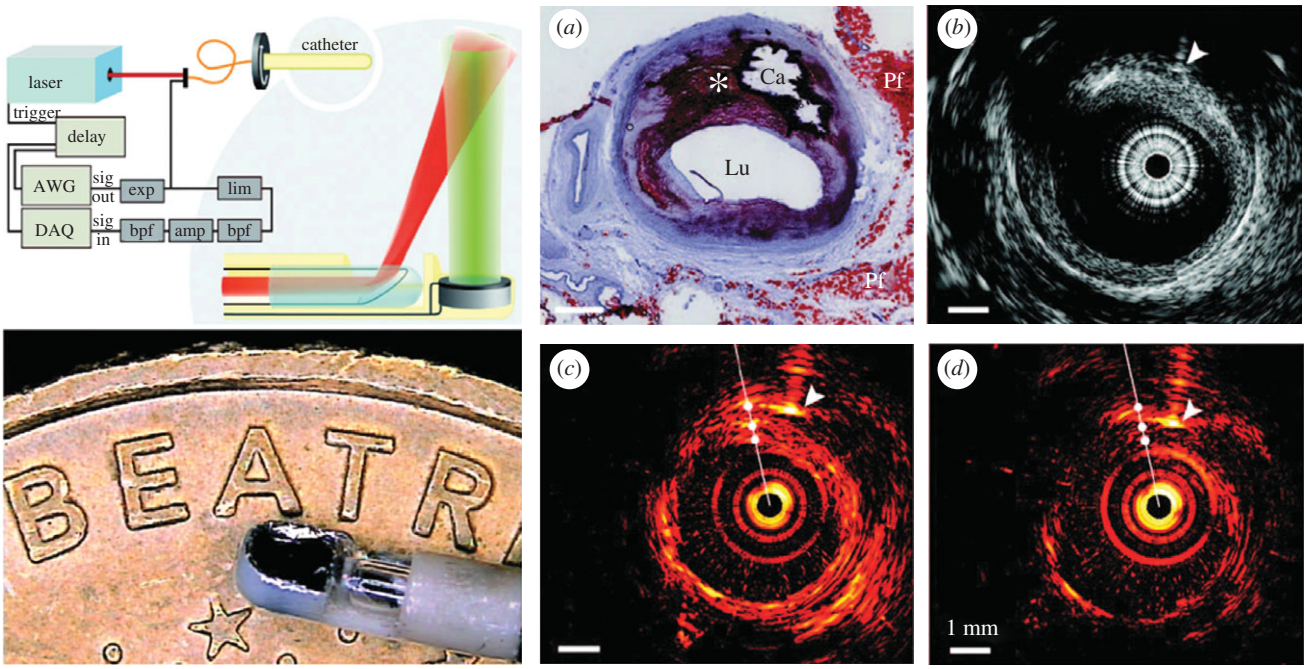

Figure 12. Dual mode intravascular PA and US imaging probe used to image *ex vivo* human coronary arteries [127]. Left panel: (upper) schematic of experimental set-up. (lower) photograph of distal end of catheter. Right panel: (*a*) Histological section showing a lipid-rich plaque (asterisk) and a region of calcification (Ca). Lu, lumen; Pf, peri-adventitial fat. (*b*) IVUS image, (*c*) intravascular PA image obtained using an excitation wavelength of 1210 nm (high lipid absorption) and (*d*) intravascular PA image obtained using an excitation wavelength of 1230 nm (low lipid absorption).

components by tuning the excitation laser wavelength to the absorption features of their constituent chromophores. For example, as discussed in the previous section, by exciting at a wavelength that corresponds to the 1210 nm characteristic lipid absorption peak, the presence of lipid-rich atheromatous plaques can be identified [131,132]. Although useful, it is possible to go much further than this type of simple contrast enhancement. By acquiring images at multiple wavelengths and undertaking a spectroscopic analysis, the concentration of specific chromophores can be quantified in a manner analogous to conventional optical transmission spectroscopy [133] assuming that the spectral characteristics of the chromophores and scatterers present are known. For example, the absorption spectrum of blood at visible and NIR wavelengths is strongly dependent upon its oxygen saturation (sO_2), a consequence of the significant spectral differences between oxyhaemoglobin (HbO_2) and deoxyhaemglobin (HHb) as shown in figure 1. With knowledge of these spectral differences, it is then possible to quantify the concentrations of HbO_2 and HHb and estimate sO_2, an important physiological parameter intimately related to a broad range of pathophysiological processes such as angiogenesis and tissue inflammatory processes. As well as imaging endogenous chomophore concentrations, spectroscopic techniques provide a means of detecting and quantifying the accumulation of targeted contrast agents used in PA molecular imaging. Here, a spectrally distinct absorber such as a dye molecule or nanoparticle is tagged to targeted compound that binds to a disease-specific receptor such as a cell-surface protein or enzyme. Using spectroscopic methods to quantify the local accumulation of the contrast agent can therefore provide information about disease processes at a cellular or molecular level.

As the above indicates, PA spectroscopy is an important adjunt to PA imaging techniques in that it provides it with a functional and molecular imaging capability. However, achieving absolute or even relative quantification of chromophore concentrations using PA spectroscopy represents a significant challenge [21,134]. Although as discussed in §2, PA contrast is often said to be 'absorption-based', this does not mean that it is directly proportional to the absorption coefficient—a PA image is a representation of the absorbed optical energy distribution not the absorption coefficient distribution as sometimes assumed. The absorbed optical energy at a point is the product of the local absorption coefficient and the fluence, the latter being dependent on the distribution of absorption and scattering coefficients over the entire illuminated tissue volume. The spectra of all the different chromophores and scatterers in this volume will therefore, to some extent, be encoded onto the absorbed energy spectrum at a specific point. An obvious example occurs when two spectrally distinct absorbers are located such that one lies directly beneath the other. Since the light will have passed through the top absorber to reach the one beneath it, the absorbed energy spectrum of the latter will be composed of the spectral characteristics of both. Indeed given that in tissues, a photon can be scattered from any point to another, this type of spectroscopic cross-talk can occur even if two absorbers are located side by side at the same depth or indeed, if there is significant backscattering, from a deeply lying absorber to another situated directly above it. As a consequence, the problem of recovering chromophore concentrations differs

from simple conventional optical transmission spectroscopy [133]. In the latter, the signal is assumed to be directly proportional to the absorption coefficient which allows the problem to be formulated as a set of simultaneous linear equations (one for each wavelength) which can be efficiently inverted to recover the chromophore concentrations. Since PA image contrast is not proportional to the absorption coefficient however, attempting to apply this type of simple linear inversion pixel-by-pixel to a set of multi-wavelength PA images is unlikely to be successful [25]. There are some exceptions. For example, if the target is optically homogeneous [135] or if the chromophore of interest is surrounded by chromophores that are either of uniform spectral characteristics or relatively weakly absorbing or both. However, these conditions rarely exist in biological tissues *in vivo*. An exception in which a simple linear spectroscopic inversion can be valid occurs when imaging highly superficial features within a few hundred micrometres of the surface as in OR-PAM (§4.2.2). Under these conditions, the wavelength dependence of the external light distribution can largely be ignored. The assumption that image contrast is directly proportional to the absorption coefficient can then reasonably be made and the quantitative measurement of chromophore concentrations using a linear inversion becomes possible.

It is now widely accepted that addressing the corrupting influence of the wavelength dependence of the fluence distribution is key to achieving accurate quantitative spectroscopic measurements. One approach is to modify the above-mentioned linear spectroscopic decomposition by incorporating empirical correction or calibration factors that account for the wavelength dependence of the external light distribution. For example, it has been suggested that the spectral characteristics of the tissue overlaying the region of interest could be accounted for by measuring the light transmission as a function of wavelength through a sample of excised tissue of the same type [136]. Another method of obtaining the same type of information involved measuring the PA spectrum of a black plastic absorber (of presumably uniform or known spectral characteristics) embedded beneath the skin of a live mouse at the depth of interest [96,101]. The drawback with such empirical correction factors, apart from the invasive and clinically inapplicable methods required to obtain them, is that they are highly dependent upon the tissue structure, composition and physiology, particularly perfusion and oxygenation status. Given that these vary significantly between different tissue types and over time, this inevitably limits their general applicability. A fundamentally different approach, and one that has the potential to avoid these limitations, is to use a nonlinear model-based inversion scheme. In this, the wavelength-dependent light distribution is accounted for, not by using empirical correction factors, but through an explicit mathematical representation of light transport within a forward model. The model provides multi-wavelength images of PA images or signals as a function of the spatial distribution of chromophore concentrations. The latter are then estimated by inverting the model, achieved by varying the chromophore concentrations until the difference between the measured images and those predicted by the model is minimized. Because the model can be formulated as a function of an arbitrary spatial distribution of any number of chromophores, this approach is applicable, in principle, to any tissue geometry or type, albeit at some computational expense especially if implemented in three dimensions. This method has been demonstrated experimentally using simulated data [137] to obtain two-dimensional maps of chromophore concentrations. It has also been used (in a reduced form to minimize computation time), for the quantitative measurement of HbO_2 and HHb and blood sO_2 from single-point PA signals generated in tissue mimicking phantoms [25] and subsequently for the recovery of two-dimensional images of chromophore concentrations [138]. An alternative strategy is to attempt to use a light transport model to recover absorption coefficient images at individual wavelengths and then apply a linear inversion, pixel by pixel, to recover chromophore concentrations. However, because of the absorption-scattering non-uniqueness associated with absorbed energy images [137], it is not generally possible to obtain absorption coefficient images at a single wavelength without incorporating additional information such as the scattering distribution, which is not usually known, or fluence measurements obtained from another imaging modality (e.g. optical tomography [139,140]), which incurs additional experimental complexity. The method described above overcomes this by fitting the forward model to all of the measured multi-wavelength PA images simultaneously—in essence the additional information provided by the known spectral characteristics of the constituent chromophores and scatterers ameliorates the non-uniqueness. Xiao *et al.* [141] describe a different model-based inversion scheme and suggest that both chromophore concentrations and sound speed can be recovered.

Other methods that seek to compensate for the corrupting effect of the wavelength dependence of the fluence distribution are based on the use of additional information. One of these relies on the introduction of a contrast agent of known absorption spectrum [142]. Another employs diffuse reflectance spectroscopy [143] to estimate tissue optical properties which are then used in a light propagation model to correct for fluence changes. The use of diffuse optical tomography to independently estimate the fluence as mentioned above has also been explored [139,140].

5.2. Photoacoustic Doppler flowmetry

A further functional capability is the measurement of blood flow velocity using Doppler flowmetry techniques. This would be useful in its own right, for example, to study flow in tumour vessels where the tortuous nature of the microvasculature can lead to chaotic and variable blood flow which can inhibit therapeutic response. However, if both blood flow and sO_2 can be measured simultaneously (the latter as described in §5.1), there is also the prospect of being able to estimate oxygen delivery and thus provide a measure of oxygen consumption—an important physiological parameter

related to tissue metabolism that is difficult to measure non-invasively using other methods without employing contrast agents. PA flow measurements can be made in a manner analogous to conventional Doppler ultrasound—that is to say by recovering the Doppler frequency, phase or time shift encoded onto PA waves emitted by moving red blood cells (RBCs). Unlike Doppler ultrasound, however, the detected acoustic signal is emitted by the blood cells as opposed to being weakly reflected from them. This offers significant SNR advantages especially when measuring flow in microvessels as these exhibit low echogenicity. Furthermore, Doppler ultrasound measurements of the relatively low flow speeds (less than 50 mm s^{-1}) in microvessels can be corrupted by the much larger backscattered signal from the surrounding tissue which can move at comparable speeds owing to respiratory or cardiac motion. In PA Doppler flowmetry, this is less problematic owing to the much stronger optical absorption of blood compared with that of the vessel wall and surrounding tissue. For these reasons, PA Doppler is envisaged primarily for the measurement of the low flow velocities in the microvasculature, not fast moving blood in the major arteries which is currently well served by conventional pulsed wave Doppler ultrasound.

Although the principles of PA Doppler flowmetry were outlined over a decade ago [144], it is only relatively recently that it has been demonstrated experimentally. PA measurements of velocity in a tissue-mimicking phantom have been obtained by recovering Doppler frequency shifts using continuous wave (CW) excitation [145,146]. However, in common with CW Doppler ultrasound, this approach cannot readily provide depth-resolved measurements. The use of pulsed excitation overcomes this limitation. Time-resolved spectral analysis of toneburst excited PA waves [147] has been successful in quantifying Doppler frequency shifts for velocities between 3.5 and 200 mm s^{-1} in phantoms [148]. There is inevitably a velocity-spatial resolution compromise with this method—a long-duration toneburst provides high spectral and therefore velocity resolution but at the cost of spatial resolution. In Sheinfeld *et al.* [148], a toneburst duration of 3 μs was used. This provided a velocity resolution of 1.5 mm s^{-1} but a relatively low depth resolution of 4.5 mm. Although a source emitting in the telecoms C-band (1530 nm–1565 nm) was used to demonstrate the concept in a phantom [148], the limited availability of quasi-CW-modulated laser sources with sufficient output power at wavelengths suitable for *in vivo* use (i.e. <900 nm) may present a practical limitation. An alternative Doppler flowmetry method based upon pulsed excitation and time correlation processing has also been explored [149,150]. This approach, inspired by time correlation ultrasound flowmetry [151,152], relies up on measuring the change in the time of arrival of successive photoacoustic pulses emitted by a moving cluster of RBCs using the cross-correlation function. By using short (nanosecond) laser pulses, it offers high spatial resolution and can employ the type of readily available pulsed Q-switched lasers used routinely in PA imaging. Velocity range and resolution are scalable with excitation pulse separation: for a pulse separation of 5 ms and an upper limit of 180 mm s^{-1}, the velocity resolution has been estimated to be ± 1 mm s^{-1} [151]. To date, depth-resolved PA Doppler flowmetry using the acoustically defined PA modes (AR-PAM or PAT) has not been demonstrated in blood, only in tissue-mimicking phantoms [147–150]. The challenge in making measurements in blood relates to its optical heterogeneity. If the spatial separation between individual RBCs or clumps of RBCs is small compared with the minimum detectable acoustic wavelength, blood will approximate to a spatially homogeneous absorber and compromise the ability of time correlation and possibly other time-domain methods to make velocity measurements. Whether this will prove to be fundamentally limiting remains to be seen. The success of pulsed wave Doppler ultrasound [152] and cross correlation pulse-echo ultrasound measurements of blood flow [151] suggests that at least some optimism is warranted.

In the optically defined mode, OR-PAM, however, the spatial heterogeneity issue does not present a fundamental limitation. This is because the excitation spot size (approx. a few micrometres) is comparable to that of a single RBC allowing the spatial heterogeneity in the optical absorption of blood to be directly resolved. As a consequence, measurements of blood flow have successfully been demonstrated *in vivo*. One method is based on recovering the acoustic bandwidth broadening arising from the frequency difference between the extremities of a wavefront emitted by an absorber moving orthogonal to the axis of a focused transducer [153]. The frequency shift is estimated by computing the autocorrelation of sequentially acquired A-lines produced by successive laser pulses. Being a pulsed excitation scheme, spatially resolved flow measurements can be made. This approach has been demonstrated *in vivo* for measuring velocities up to approximately 7.4 mm s^{-1} with a resolution of 0.1 mm s^{-1} and thus within the velocity range of blood flow in microvessels [154]. It has also been used to obtain two-dimensional maps of flow in the vasculature of the mouse ear and combined with spectroscopic measurements of sO_2 to estimate changes in the metabolic rate of oxygen [155], a measure of tissue oxygen consumption. The challenge ahead in PA Doppler flowmetry is to translate the success of OR-PAM flowmetry to the acoustically defined modalities AR-PAM and PAT in order to make flow measurements beyond the optically defined 1 mm penetration depth limit of OR-PAM.

5.3. Photoacoustic thermometry

The temperature dependence of the Grüneisen coefficient, a measure of the thermo-mechanical efficiency of the PA generation process, provides a means of non-invasively obtaining maps of temperature distributions in tissue. This has application in thermotherapy in which heat is used to ablate tissue pathologies such as tumours. In photothermal cancer therapy, for example, a targeted contrast agent such as highly absorbing conjugated gold nanoparticles that selective bind to tumour-specific cells is systemically introduced. The tumour is irradiated with high-intensity 'therapeutic' CW laser light at a wavelength at which the contrast agent is strongly

absorbing. Only those tumour cells to which the highly absorbing contrast agent has an affinity to will be heated and therefore destroyed leaving the surrounding normal tissue unaffected. PA imaging could be used in two ways to plan and monitor the treatment. Firstly, a PA image is directly proportional to absorbed optical energy. Thus if an image is acquired prior to therapy, it will provide an estimation of those parts of the tumour that will be heated when the 'therapeutic' CW laser light is delivered to the tumour. Secondly, by acquiring PA images during the therapeutic heating phase, the temperature rise and thus the thermal 'dose' could be monitored in real time. In this way, it would be possible to determine which regions of the tumour had been heated to a temperature beyond the threshold for cell death and adjust the treatment parameters accordingly. The ability to map temperature could similarly be applied to the monitoring of HIFU therapy for treatment parameter optimization, as described in §6.1.5. Several studies have been undertaken to explore the temperature dependence of time-resolved PA signals measured at a single point in phantoms and *ex vivo* tissue samples [156–158]. In addition, a study that demonstrated the potential to obtain two-dimensional maps of optically induced temperature rises in gold nanoparticles embedded in *ex vivo* tissue samples illustrates the potential for non-invasive monitoring of photothermal therapy [78]. The temperature resolution reported in these studies is of the order of 0.15°C.

6. BIOMEDICAL APPLICATIONS

6.1. Clinical

6.1.1. Breast imaging. Imaging breast cancer is an important potential clinical application of PAT. It is based on the hypothesis that the increased optical absorption arising from the higher vascularity of a tumour will be revealed as a region of elevated contrast on a PA image that can then be used to aid tumour detection and diagnosis [6,27,159–161]. In addition, the ability of PA imaging to map blood oxygenation, which may provide an indication of therapeutic response, can be exploited to help plan and monitor treatment. The identification of sentinel lymph nodes for needle biopsy guidance via the accumulation of an injected optically absorbing contrast agent is a further application that has been investigated [29,33,162,163]. Pulsed microwaves can also be used [7,164] instead of, or in addition to [74,165], optical excitation. Here, increased RF absorption owing to the higher conductivity provided by elevated levels of ionic water content, a consequence of the increased haemoglobin concentration and other proteins associated with cancer, offers a potential discriminatory mechanism that is complementary to that provided by optical excitation. The use of microwave radiation also offers the prospect of achieving greater penetration depth. Combining PA imaging with pulse-echo ultrasound [29,166] may provide a further source of contrast via differences in acoustic impedance. A key challenge in breast cancer imaging is the large penetration depths required (approx. 6 cm) although several studies using NIR optical [27,167] or microwave excitation [7,165] suggest this is feasible. A variety of instrument configurations have been developed including the hemispherical PAT detection geometry depicted in figure 4 for high-speed whole breast imaging [27] or cylindrical geometries for two-dimensional cross-sectional imaging [74,75,165] of the breast. A planar geometry has also been used in the Twente Photoacoustic Mammoscope [159–161]. In this scheme, the breast is lightly compressed between a glass plate and a two-dimensional 590-element PVDF array. The system has been evaluated in a small-scale pilot clinical study [160]. Regions of increased absorption were observed in the PA images acquired and attributed to tumour vascularization. A hand-held commercial US probe comprising a linear array and a fibre bundle to deliver the excitation light that can be moved around the breast providing two-dimensional PA and US images in real time has been developed. It has been evaluated using an animal model for the sentinel lymph node detection application referred to above [29,166]. Although the clinical utility of PA breast imaging has yet to be established with no major clinical studies undertaken to date, meeting the basic requirements in terms of range, resolution and the patient–instrument interface for at least some applications appears feasible.

6.1.2. Skin. Imaging the skin is a relatively undemanding application as the penetration depth required is modest and well within that achievable by PA imaging as illustrated in figures 8–10. Furthermore, a variety of PAT and AR-PAM instruments in one form or another have already been developed that have the required performance for visualizing the vasculature and other features in the skin [44,83,85,95]. The potential to image the structure and function of the dermal and sub-dermal vasculature as well as melanin content suggest PA imaging is applicable to the clinical assessment of skin pathologies: for example, to provide a more accurate diagnosis and staging of tumours such as malignant melanomas and help plan their surgical excision. Other potential applications include the assessment of burn depths, wound healing, plastic surgery procedures and superficial soft tissue damage such as pressure sore onset and ulceration. Some of these applications have explored in mouse models initially, although none as yet clinically. For example, preclinical studies have shown that skin burn depths [168,169] and melanomas [101,170] can be identified. Most human studies have demonstrated the ability of PA imaging to visualize the skin microvasculature rather than characterize specific pathologies. Favazza *et al.* [94], however, describe a study in which it is shown that the structure of a benign-pigmented skin lesion can be imaged—the implication being that PA imaging could be used to provide tumour volume, depth and thickness as an aid to the clinical assessment of skin tumours.

6.1.3. Cardiovascular. As described previously, the strong absorption peak at 1210 nm of lipids offers the prospect of identifying lipid-rich atheromatous plaques which can exhibit an increased propensity to rupture.

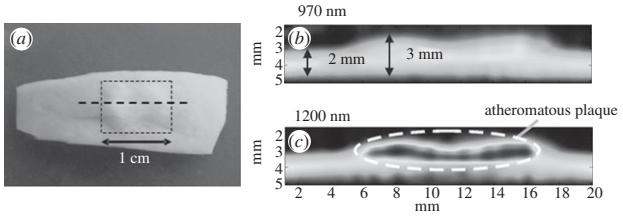

Figure 13. Photoacoustic imaging of lipid-rich atheromatous plaques [132]. (*a*) Photograph of human aorta sample with raised plaque. The horizontal dotted line represents the photoacoustic scan line. (*b*) Two-dimensional photoacoustic image obtained at 970 nm (low lipid absorption), (*c*) photoacoustic image obtained at 1200 nm (high lipid absorption) showing the high contrast owing to increased lipid content within plaque.

Such vulnerable plaques can then form an occlusive thrombus which may lead to heart attack or stroke. The coronary artery wall could potentially be imaged using a miniature intravascular sideways looking probe in a manner analogous to conventional IVUS as described in §4.3. However, the spectroscopic capability of PA imaging offers the prospect of providing more specific and quantitative information about plaque composition than ultrasound alone can provide. Several *ex vivo* studies [127,131,132,171] have demonstrated the potential to reveal the location of lipid-rich plaques using multi-wavelength imaging as illustrated in figure 13. While lipids present the most obvious source of differential contrast, other diagnostically relevant plaque constituents such as calcium deposits, macrophage content and fibrous material may also have sufficiently distinctive absorption spectra to allow their content to be identified and quantified. To detect macrophages (which may be implicated in the formation of the lipid pool in vulnerable plaques), a novel scheme based on the plasmon resonance coupling-induced wavelength shift in the absorption spectrum of gold nanoparticles has been described [172]. In this approach, gold nanoparticles are taken up by macrophages. The close proximity of the nanoparticles within the cell results in the wavelength shift owing to plasmon resonance coupling. Nanoparticles outside the cell are not in sufficiently close proximity to each other to produce the shift and can therefore be differentiated from those internalized in the cell. A further application is imaging stent placement during surgical insertion and thereafter in follow up. Figure 14 shows a combined PA and US volumetric image of a stent inserted in a phantom [173]. Non-invasive cardiovascular applications that have been proposed include the detection of deep vein thombosis [174] in the venous system and the characterization of carotid artery plaques [175].

6.1.4. Opthalmology. The absorption-based contrast of PA imaging lends it to mapping the structure and oxygenation status of the retinal vasculature which is of interest in studying conditions such as age-related macular degeneration and diabetic retinopathy. Additionally, it offers the prospect of imaging melanin content in the RPE which is relevant to the study of the ageing process. Several

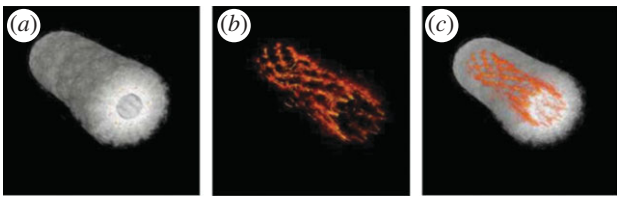

Figure 14. Combined ultrasound and PA imaging of a coronary artery stent embedded in a tissue phantom [173]. (*a*) Ultrasound image, (*b*) photoacoustic image, (*c*) fused ultrasound and photoacoustic image.

preclinical animal studies have been undertaken. A dual-mode OR-PAM-OCT instrument has been developed [120] and used to obtain *in vivo* images of the retinal vasculature, optic disc and underlying RPE (figure 15(*a*–*c*)). As well as imaging retinal blood vessels in there is further scope to visualize the structure and sO_2 of the iris microvasculature and related abnormalities as shown in figure 15(*d*) [121]. Silverman *et al.* [176] describe an OR-PAM scheme combined with a high-frequency pulse-echo ultrasound imaging capability. Another study obtained PA and US images of the eye using a dual-mode AR-PAM-US scanner revealing a greater variety of ocular anatomy (the cornea, lens iris as well as the retina, RPE and choroid) albeit with lower resolution [177].

6.1.5. HIFU monitoring. Key to the success of HIFU cancer therapy are (i) accurate identification of the tumour region to be treated, (ii) ensuring that the HIFU beam is delivered with sufficient spatial precision and selectivity to the ROI, (iii) monitoring the tissue status during the treatment via its temperature time course or through the measurement of temperature-dependent physical properties of the tissue and (iv) post-treatment assessment of the extent of tissue ablation. PA imaging offers the opportunity to address all four requirements. First, the increased vascularity of a tumour provides intrinsic PA image contrast that can be exploited to locate the tumour. Once located, accurate targeting of the HIFU beam is required so that it selectively destroys the tumour with minimal collateral damage to the surrounding tissue. However, spatial heterogeneities in sound speed can distort the HIFU wavefront in such a way that it is not brought to a tight focus, thus compromising targeting accuracy. There is the potential to mitigate this by using the detected PA signals in conjunction with time-reversal methods [178–180]. This involves transmitting the measured PA waveforms at each detection point in temporally reversed order from an array of HIFU transducers, ideally the same ones that detected the PA signals. The wavefront distortion produced by the sound speed variations will be unravelled by the time-reversal process so that the transmitted HIFU field converges on the tumour. Since the PA waves originate from the tissue region that is required to be ablated, a high degree of targeting accuracy should be achievable. Preliminary phantom studies have been undertaken demonstrating the feasibility of this approach [178,180]. There are two approaches which could be used either

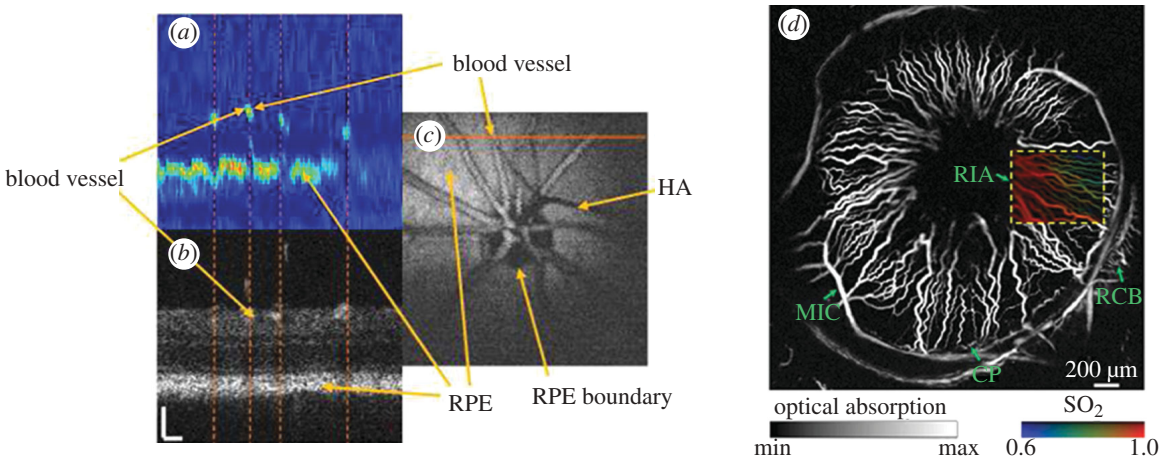

Figure 15. *In vivo* photoacoustic ocular imaging: (*a*) PA vertical B-scan image acquired along the horizontal red line in (*c*) showing retinal blood vessel and the underlying retinal pigment epithelium (RPE) in the rat eye [120]. (*b*) OCT image acquired simultaneously showing corresponding features [120], (*c*) lateral MIP showing the retinal vasculature over the optic disc. HA signifies shadowing owing to hyaloid artery remnant [120]. (*d*) Lateral MIP image of iris vasculature in mouse eye [121]. Dual wavelength spectroscopy was used to map oxygen saturation over the rectangular region indicated by the yellow dotted outline. (*d*) CP, ciliary process; MIC, major iris circle; RCB, recurrent choroidal branch and RIA, radial iris artery.

individually or together in a complementary fashion to non-invasively monitor treatment progression. The first exploits the temperature dependence of the Gruneisen coefficient [78,156–158] to non-invasively image the spatial–temporal evolution of the heating and cooling phases of the treatment [181]. The second approach is based on tracking changes in the optical and thermo-mechanical properties of the tissue during and after treatment to assess tissue ablation. Several studies using *ex vivo* tissue samples have shown that the optical properties of tissues are temperature-dependent, particularly beyond the temperature at which coagulation occurs when optical scattering increases significantly [182–184]. These studies suggest that HIFU exposure should result in a local and permanent increase in PA image contrast once beyond this temperature. However, a recent study in which an HIFU lesion was induced in the kidney of a live mouse appeared to show reduced PA image contrast [185] at 1064 nm. A possible explanation is that although scattering may have increased, the ablative process induced a greater reduction in the absorption by water or blood, the two dominant chromophores at 1064 nm. The blanching effect of HIFU that is visually apparent on highly vascularized tissues would seem to be consistent with this. However, another *in vivo* mouse study [186], reported enhanced PA image contrast as a result of HIFU exposure although the use of gold nanorods to provide contrast in the ROI may be a complicating factor precluding direct comparisons. It has also been shown that it is possible to image an HIFU lesion in *ex vivo* tissues using microwave excitation, the source of contrast being thermally induced changes in tissue conductivity due to water evaporation [187].

7. PRE-CLINICAL

PA imaging has a role to play as a non-invasive investigative tool for characterizing small animals such as mice or rats. These are widely used as a research platform for studying human disease processes and to develop new therapies. PA imaging is particularly well suited to this application. The small size of the animal means that the penetration depth requirements are not excessively challenging enabling high SNR to be achieved. The modest spatial scale also allows the PA signals to be recorded around the whole body of the animal, thus providing the necessarily large angular detection aperture for a high-quality image reconstruction. These factors have enabled high-resolution anatomical images to be obtained with high contrast as illustrated in figures 5 and 6.

A key application is the characterization of small-animal models of brain injury and disease processes, particularly those that require studying vascular anatomy and function such as stroke, epilepsy and traumatic brain injury. A number of studies have been undertaken using all three PA imaging modes. PAT has been used to image the vascular anatomy of the mouse brain [64,66,70,89], the haemodynamic response due to whisker stimulation [64] and epileptic events [65]. AR-PAM has been used to study temporal variations in cortical blood oxygenation by altering the inspired oxygen fraction to induce hypoxia and hyperoxia [188]. Haemodynamic changes due to electrical stimulation have also been investigated [110]. OR-PAM can be used for small-animal brain imaging, but unlike PAT and AR-PAM, requires removal of the scalp. It has been used to map sO_2 at capillary level in the mouse brain [117]. Other OR-PAM studies have focused on demonstrating that spatial–temporal haemodyamic events such as vasomotion and vasodilation [109] can be monitored in the mouse. Maps of blood sO_2 and flow over the vasculature have also been acquired with a view to estimating MRO_2 [155].

Mouse models are also used extensively to study the pathophysiology of a variety of tumours to aid the preclinical development of new cancer therapies. Characterizing the supplying tumour vasculature is key

to this endeavour. PA imaging offers the prospect of being able to achieve this through its ability to non-invasively map the structure, oxygenation and flow status of tumour vasculature, all of which have a major impact on tumour development and therapeutic response. Several preliminary studies have been undertaken with the aim of imaging abnormal tumour vessels [189] or the evolution of tumour vasculature over time owing to angiogenesis [67,190]. Several other studies have shown that subcutaneous melanomas can be visualized, either by exploiting intrinsic contrast [170] or through the use of a targeted contrast agent [191].

Other preclinical studies that have been undertaken include imaging the vascular anatomy of the mouse embryo [50,90] studying cardiovascular dynamics [69] and kidney perfusion [68].

As well as providing structural and functional information; there is the prospect of using PA imaging to help elucidate disease processes at a cellular or molecular level through the use of exogenous contrast agents and reporter genes—a detailed review of PA molecular imaging is provided in Kim *et al.* [14]. Briefly, there are two principal approaches. The first involves systemically introducing a targeted contrast agent that selectively accumulates at a disease-specific receptor such as a cell-surface protein or enzyme. The absorbing component of the contrast agent can be an organic dye such as ICG or a fluorophore [192] (the absorption band of the fluorophore providing the source of contrast). The advantage of using fluorophores is that they have been extensively developed for fluorescence molecular imaging and can readily be conjugated to target a wide range of specific cellular and intracellular receptors. Their disadvantages are a relatively small absorption cross section and a propensity to bleach or otherwise degrade when irradiated with the high peak powers characteristic of PA excitation laser pulses. Metallic nanoparticles such as nanoshells, nanorods and other structures provide a promising alternative. Their plasmon resonance absorption cross sections can be orders of magnitude higher than dye molecules and, by adjusting their geometrical parameters, their peak absorption wavelength can be tuned to NIR wavelengths. Furthermore, in some cases, nanoparticulate structures (e.g. single-walled carbon nanotubes) can exhibit higher photostability than organic dyes. Specific targeting using contrast agents has now been demonstrated *in vivo* in tumours using carbon nanotubes [100,193], gold nanorods [194] and cages [191] to provide selective contrast. The second method involves incorporating engineered reporter genes that express optically absorbing proteins in mice. This offers the prospect of studying the role of genetic processes in disease pathways. LacZ gene expression has been detected by PA imaging via the change in the optical absorption of X-gal when catalysed by the LacZ-encoded enzyme β-galactosidase [195]. However, achieving this required the local injection of the X-gal substrate into the ROI. PA imaging of cells expressing flourescent proteins (the absorption band of the protein providing the PA image contrast) has been demonstrated in a non-interventional manner but only in the relatively transparent Zebrafish or small-scale *Drosophila* (fruitfly) pupa [196]. New reporters that absorb at longer wavelengths in the NIR are required in order to achieve the penetration depths required for imaging in small animals such as mice.

8. SUMMARY

In terms of obtaining high-quality three-dimensional anatomical images over a range of spatial scales, the feasibility of PA imaging has surely been demonstrated. Major progress in the development of instrumentation, image reconstruction methods and functional and molecular PA imaging has been made in the last 5 years and the translation to clinical and other applications has begun. However, there are a number challenges to be addressed if the full potential of the technique is to be realized.

The challenges ahead in terms of instrument development lie at both a component and system level. At a component level, there is a need for highly sensitive suitably broadband receivers for PA detection, a need that may be met by advanced piezoelectric transducers, based on single-crystal materials or new piezocomposites designed specifically to meet the detection sensitivity and bandwidth requirements of PA imaging rather than being non-optimally adapted from other ultrasound applications. New approaches based on optical ultrasound sensing such as the FP sensor described in §4.1.1 or other methods [197] may also play a role in this respect. The lack of suitable laser systems is widely recognized as a major bottleneck in the clinical translation of the technique. For PAT and AR-PAM, commercially available Q-switched Nd : YAG pumped OPO, Ti Sapphire or dye laser systems have proved to be extremely effective for demonstrating feasibility in a laboratory environment. However, their large size, lack of practical utility (e.g. the need for re-alignment) and requirement for external cooling systems as well as the need to be operated by technically experienced personnel inhibits their practical use, particularly within a clinical environment. Furthermore, those systems that are able to provide the milliJoule pulse energies required for PAT tend to have low PRFs (less than 50 Hz). As well as limiting image frame rates this inhibits the implementation of time domain signal processing techniques such as pulsed Doppler flowmetry that require high PRFs. Slow tuning speeds or insufficient tuning range also inhibits the practical application of spectroscopic methods and thus the functional and molecular imaging capability of the technique. There are some signs that progress is being made in this direction. Compact, portable, high PRF fibre laser systems are beginning to find application [99,198] although, with one exception [199], only in OR-PAM as the pulse energies of most currently available systems are insufficient for use in AR-PAM and PAT. Laser diode-based systems have been also demonstrated for superficial imaging applications [200,201]. Although advances in high-power pulsed laser diode technology and novel signal processing schemes are likely to increase their practical utility, the fundamental peak power limit imposed by the facet damage threshold is likely to preclude their

use for deep-tissue PAT imaging using pulsed excitation. Alternative excitation schemes such as those based on frequency domain methods may provide an opportunity to overcome this limitation [10–12].

At a systems level, the challenge in PAT is to achieve real-time image frame rates without excessively compromising SNR. For PAT, there is a fundamental limit. Irrespective of the availability of suitable lasers, average power safety-related considerations mean that to achieve real time frame rates and the highest possible SNR, a PRF in the low tens of hertz and parallel detection, signal conditioning and acquisition on all channels is ideally required. Operating at a higher PRF and multiplexing down to reduce the number of truly parallel channels can be achieved as in conventional US. However, it results in reduced SNR as the pulse energy has to be reduced to limit average power. For three-dimensional imaging, which can require two-dimensional array channel counts of the order of 10^4 [3], the cost of a fully parallel system would be prohibitive. The challenge, therefore, is to find the optimal compromise between PRF and thus SNR, multiplexing ratios and frame rates. These considerations apply principally to PAT. Different considerations in respect of PRF and acquisition speed apply to the PA microscopy modes which are not readily parallelizable.

Spectroscopic techniques are key to realizing the functional and molecular imaging capability of PA imaging. Although much progress has been made in the development of inversion algorithms, addressing the corrupting influence of the wavelength dependence of the light fluence remains a major challenge. Model-based inversion schemes that fully account for the physics involved in the PA signal generation and detection process have promise but in their most general form are still too computationally expensive for many practical applications. Limiting the spatial domain, constraining the solution with additional information, prior or otherwise, and developing ad hoc, albeit rigorously validated, approximations for specific applications may yield progress with these methods. Accurate quantitation of chromophore concentrations is the ultimate goal of quantitative PA spectroscopy and essential for the measurement of physiological parameters such as blood sO_2. However, spectroscopic methods are important even if it is required only to detect rather than quantify the presence of specific chromophores. This is especially so in molecular imaging given the relatively low concentrations that targeted molecular imaging contrast agents or genetically expressed reporters are likely to accumulate in. Accurate spectroscopic inversion or unmixing techniques will be essential for the sensitive detection of molecular imaging agents in the face of the overwhelming PA contribution from haemoglobin.

In PA molecular imaging, specific targeting using systemically introduced contrast agents has been demonstrated and much effort is now being devoted to optimizing the labelling component of the agent using a variety of nanoparticulate structures. The use of engineered genetic reporters has much promise having been demonstrated using existing fluorescent reporters to provide PA contrast. The challenge ahead here is to develop genetically expressed proteins that absorb at longer wavelengths in order to enable greater penetration depth to be achieved, are stable under the high peak power of PA excitation laser pulses and can be expressed by mammalian cells.

In terms of biomedical application, preclinical PA imaging is already becoming established as a useful tool and beginning to be applied as opposed to merely being demonstrated. Translation to clinical application is less well advanced, perhaps inevitably with relatively few clinical studies having been undertaken, in part due to the more stringent requirements in terms of acquisition speed, portability and patient–instrument interface considerations. However, with the emergence of dedicated clinical systems, especially those based on existing diagnostic ultrasound scanners, the rate of progression towards clinical application in oncology, dermatology, cardiovascular medicine and other specialities is set to increase in the near future.

The author acknowledges helpful discussions with and contributions from members of the UCL Photoacoustic Imaging Group, among them Ben Cox, Jan Laufer, Thomas Allen, Edward Zhang, Jo Brunker and Bradley Treeby. The author was supported by an EPSRC Leadership Fellowship.

REFERENCES

1 Bell, A. G. 1880 On the production and reproduction of sound by light. *Am. J. Sci.* **20**, 305–324.
2 Tam, A. 1986 Applications of photoacoustic sensing techniques. *Rev. Mod. Phys.* **58**, 381–431. (doi:10.1103/RevModPhys.58.381)
3 Kruger, R., Liu, P. & Appledorn, C. 1995 Photoacoustic ultrasound (PAUS)—reconstruction tomography. *Med. Phys.* **22**, 1605–1609. (doi:10.1118/1.597429)
4 Esenaliev, R. O., Karabutov, A. A., Tittel, F. K., Fornage, B. D., Thomsen, S. L., Stelling, C. & Oraevsky, A. A. 1997 Laser optoacoustic imaging for breast cancer diagnostics: limit of detection and comparison with x-ray and ultrasound imaging. *Proc. SPIE* **2979**, 71–82. (doi:10.1117/12.280213)
5 Hoelen, C. G., de Mul, F. F., Pongers, R. & Dekker, A. 1998 Three-dimensional photoacoustic imaging of blood vessels in tissue. *Opt. Lett.* **23**, 648–650. (doi:10.1364/OL.23.000648)
6 Oraevsky, A. A., Andreev, V. A., Karabutor, A. A., Declan Fleming, K. R., Gatalica, Z., Singh, H. & Esenalier, R. O. 1999 Laser optoacoustic imaging of the breast: detection of cancer angiogenesis. *Proc. SPIE* **3597**, 352–363. (doi:10.1117/12.356829)
7 Kruger, R. A., Miller, K. D., Reynolds, H. E., Kiser, W. L., Reinecke, D. R. & Kruger, G. A. 2000 Breast cancer *in vivo*: contrast enhancement with thermoacoustic CT at 434 MHz-feasibility study. *Radiology* **216**, 279–283.
8 Ku, G. & Wang, L. 2000 Scanning thermoacoustic tomography in biological tissue. *Med. Phys.* **27**, 1195–1202. (doi:10.1118/1.598984)
9 Beard, P. C. 2002 Photoacoustic imaging of blood vessel equivalent phantoms. *Proc. SPIE* **4618**, 54–62. (doi:10.1117/12.469848)
10 Fan, Y., Mandelis, A., Spirou, G. & Alex Vitkin, I. 2004 Development of a laser photothermoacoustic frequency-swept system for subsurface imaging: Theory and experiment. *J. Acoust. Soc. Am.* **116**, 3523–3533. (doi:10.1121/1.1819393)

11 Maslov, K. & Wang, L. V. 2008 Photoacoustic imaging of biological tissue with intensity-modulated continuous-wave laser. *J. Biomed. Opt.* **13**, 024006. (doi:10.1117/1.2904965)

12 Lashkari, B. & Mandelis, A. 2010 Photoacoustic radar imaging signal-to-noise ratio, contrast, and resolution enhancement using nonlinear chirp modulation. *Opt. Lett.* **35**, 1623–1625. (doi:10.1364/OL.35.001623)

13 Hu, S. & Wang, L. V. 2010 Neurovascular photoacoustic tomography. *Front. Neuroenergetics* **2**, 10. (doi:10.3389/fnene.2010.00010)

14 Kim, C., Favazza, C. & Wang, L. V. 2010 *In vivo* photoacoustic tomography of chemicals: high-resolution functional and molecular optical imaging at new depths. *Chem.l Rev.* **110**, 2756–2782. (doi:10.1021/cr900266s)

15 Hu, S. & Wang, L. V. 2010 Photoacoustic imaging and characterization of the microvasculature. *J. Biomed. Opt.* **15**, 011101. (doi:10.1117/1.3281673)

16 Wang, L. V. 2009 Multiscale photoacoustic microscopy and computed tomography. *Nat. Photonics* **3**, 503–509. (doi:10.1038/nphoton.2009.157)

17 Li, C. & Wang, L. V. 2009 Photoacoustic tomography and sensing in biomedicine. *Phys. Med. Biol.* **54**, R59–R97. (doi:10.1088/0031-9155/54/19/R01)

18 Xu, M. & Wang, L. V. 2006 Photoacoustic imaging in biomedicine. *Rev. Sci. Instrum.* **77**, 041101. (doi:10.1063/1.2195024)

19 Mallidi, S., Luke, G. P. & Stanislav, E. 2011 Photoacoustic imaging in cancer detection, diagnosis, and treatment guidance. *Trends Biotechnol.* **29**, 213–221. (doi:10.1016/j.tibtech.2011.01.006)

20 Cox, B. T. & Beard, P. C. 2005 Fast calculation of pulsed photoacoustic fields using k-space methods. *J Acoust. Soc. Am.* **117**, 3616–3636. (doi:10.1121/1.1920227)

21 Cox, B. T., Laufer, J. G. & Beard, P. C. 2009 The challenges for quantitative photoacoustic imaging. *Proc. SPIE* **7177**, 717713. (doi:10.1117/12.806788)

22 Hale, G. M. & Querry, M. R. 1973 Optical-constants of water in 200 nm to 200 mum wavelength region. *Appl. Opt.* **12**, 555–563. (doi:10.1364/AO.12.000555)

23 van Veen, R. L. P., Sterenborg, H. J. C. M., Pifferi, A., Torricelli, A., Chikoidze, E. & Cubeddu, R. 2010 Determination of visible near-IR absorption coefficients of mammalian fat using time- and spatially resolved diffuse reflectance and transmission spectroscopy. *J. Biomed. Opt.* **10**, 054004. (doi:10.1117/1.2085149)

24 Tsai, C. L., Chen, J. C. & Wang, W. J. 2001 Near-infrared absorption property of biological soft tissue constituents. *J. Med. Biol. Eng.* **21**, 7–14.

25 Laufer, J., Delpy, D., Elwell, C. & Beard, P. 2007 Quantitative spatially resolved measurement of tissue chromophore concentrations photoacoustic spectroscopy: application to the measurement of blood oxygenation and haemoglobin concentration. *Phys. Med. Biol.* **52**, 141–168. (doi:10.1088/0031-9155/52/1/010)

26 Xu, Z., Li, C. & Wang, L. V. 2010 Photoacoustic tomography of water in phantoms and tissue. *J. Biomed. Opt.* **15**, 036019. (doi:10.1117/1.3443793)

27 Kruger, R. A., Lam, R. B., Reinecke, D. R., Del Rio, S. P. & Doyle, R. P. 2010 Photoacoustic angiography of the breast. *Med. Phys.* **37**, 6096. (doi:10.1118/1.3497677)

28 Ku, G. & Wang, L. V. 2005 Deeply penetrating photoacoustic tomography in biological tissues enhanced with an optical contrast agent. *Opt. Lett.* **30**, 507–509. (doi:10.1364/OL.30.000507)

29 Kim, C., Erpelding, T., Jankovic, L. & Pashley, M. D. 2010 Deeply penetrating *in vivo* photoacoustic imaging using a clinical ultrasound array system. *Biomed. Opt. Exp.* **1**, 335–340.

30 Homan, K., Kim, S., Chen, Y.-S., Wang, B., Mallidi, S. & Emelianov, S. 2010 Prospects of molecular photoacoustic imaging at 1064 nm wavelength. *Opt. Lett.* **35**, 2663–2665. (doi:10.1364/OL.35.002663)

31 Beard, P. C. 2002 Photoacoustic imaging of blood vessel equivalent phantoms. *Proc. SPIE* **4618**, 54–62. (doi:10.1117/12.469848)

32 Kuchment, P. & Kunyansky, L. 2008 Mathematics of thermoacoustic tomography. *Eur. J. Appl. Math.* **19**, 191–224. (doi:10.1017/S0956792508007353)

33 Kuchment, P. & Kunyansky, L. 2011 Mathematics of photoacoustic and thermoacoustic tomography. In *Springer Handb. Math. Methods Imag.* (ed. O. Scherzer), pp. 819–865. New York: Springer.

34 Finch, D., Patch, S. K. & Rakesh, S. J. 2004 Determining a function from its mean values over a family of spheres. *SIAM J. Math. Anal.* **35**, 1213–1240. (doi:10.1137/S0036141002417814)

35 Kunyansky, L. A. 2007 Explicit inversion formulae for the spherical mean Radon transform. *Inverse Probl.* **23**, 373–383. (doi:10.1088/0266-5611/23/1/021)

36 Xu, M. & Wang, L. 2005 Universal back-projection algorithm for photoacoustic computed tomography. *Phys. Rev. E* **71**, 1–7.

37 Lam, R. B., Kruger, R. A., Reinecke, D. R., DelRio, S. P., Thornton, M. M., Picot, P. A. & Morgan, T. G. 2010 Dynamic optical angiography of mouse anatomy using radial projections. *Proc. SPIE* **7564**, 756405. (doi:10.1117/12.841024).

38 Norton, S. J. & Linzer, M. 1981 Ultrasonic reflectivity imaging in three dimensions: exact inverse scattering solutions for plane, cylindrical, and spherical apertures. *IEEE Trans. Bio-med. Eng.* **28**, 202–220. (doi:10.1109/TBME.1981.324791)

39 Kunyansky, L. A. 2007 A series solution and a fast algorithm for the inversion of the spherical mean Radon transform. *Inverse Probl.* **23**, S11–S20. (doi:10.1088/0266–5611/23/6/S02)

40 Anastasio, M. A., Zhang, J., Modgil, D. & Rivière, P. J. L. 2007 Application of inverse source concepts to photoacoustic tomography. *Inverse Probl.* **23**, S21–S35. (doi:10.1088/0266-5611/23/6/S03)

41 Xu, Y., Xu, M. & Wang, L. V. 2002 Exact frequency-domain reconstruction for thermoacoustic tomography–II: Cylindrical geometry. *IEEE Trans. Med. Imag.* **21**, 829–833. (doi:10.1109/TMI.2002.801171)

42 Köstli, K. P., Frenz, M., Bebie, H. & Weber, H. P. 2001 Temporal backward projection of optoacoustic pressure transients using fourier transform methods. *Phys. Med. Biol.* **46**, 1863–1872. (doi:10.1088/0031-9155/46/7/309)

43 Xu, Y., Feng, D. & Wang, L. V. 2002 Exact frequency-domain reconstruction for thermoacoustic tomography. I: planar geometry. *IEEE Trans. Med. Imag.* **21**, 823–828. (doi:10.1109/TMI.2002.801172)

44 Niederhauser, J. J., Jaeger, M., Lemor, R., Weber, P. & Frenz, M. 2005 Combined ultrasound and optoacoustic system for real-time high-contrast vascular imaging *in vivo*. *IEEE Trans. Med. Imag.* **24**, 436–440. (doi:10.1109/TMI.2004.843199)

45 Zhang, E. Z., Laufer, J. G., Pedley, R. B. & Beard, P. C. 2009 *In vivo* high-resolution 3D photoacoustic imaging of superficial vascular anatomy. *Phys. Med. Biol.* **54**, 1035–1046. (doi:10.1088/0031-9155/54/4/014)

46 Xu, Y. & Wang, L. V. 2004 Time reversal and its application to tomography with diffracting sources. *Phys.*

Rev. Lett. **92**, 033902. (doi:10.1103/PhysRevLett.92.033902)
47 Burgholzer, P., Matt, G. J., Haltmeier, M. & Paltauf, G. 2007 Exact and approximative imaging methods for photoacoustic tomography using an arbitrary detection surface. *Phys. Rev. E* **75**, 046706. (doi:10.1103/PhysRevE.75.046706)
48 Hristova, Y., Kuchment, P. & Nguyen, L. 2008 Reconstruction and time reversal in thermoacoustic tomography in acoustically homogeneous and inhomogeneous media. *Inverse Probl.* **24**, 055006. (doi:10.1088/0266-5611/24/5/055006)
49 Treeby, B. E., Zhang, E. Z. & Cox, B. T. 2010 Photoacoustic tomography in absorbing acoustic media using time reversal. *Inverse Probl.* **26**, 115003. (doi:10.1088/0266-5611/26/11/115003)
50 Treeby, B. E., Laufer, J. G., Zhang, E. Z., Norris, F. C., Lythgoe, M. F., Beard, P. C. & Cox, B. T. 2011 Acoustic attenuation compensation in photoacoustic tomography: application to high-resolution 3D imaging of vascular networks in mice. *Proc. SPIE* **7899**, Y178992–Y978992.
51 Paltauf, G., Viator, J. A., Prahl, S. A. & Jacques, S. L. 2002 Iterative reconstruction algorithm for optoacoustic imaging. *J. Acoust. Soc. Am.* **112**, 1536. (doi:10.1121/1.1501898)
52 Yuan, Z. & Jiang, H. 2007 Three-dimensional finite-element-based photoacoustic tomography: reconstruction algorithm and simulations. *Med. Phys.* **34**, 538. (doi:10.1118/1.2409234)
53 Rosenthal, A., Razansky, D. & Ntziachristos, V. 2010 Fast semi-analytical model-based acoustic inversion for quantitative optoacoustic tomography. *IEEE Trans. Med. Imag.* **29**, 1275–1285. (doi:10.1109/TMI.2010.2044584)
54 Patch, S. K. 2004 Thermoacoustic tomography—consistency conditions and the partial scan problem. *Phys. Med. Biol.* **49**, 2305–2315. (doi:10.1088/0031-9155/49/11/013)
55 Xu, Y., Wang, L. V., Ambartsoumian, G. & Kuchment, P. 2004 Reconstructions in limited-view thermoacoustic tomography. *Med. Phys.* **31**, 724–733. (doi:10.1118/1.1644531)
56 Cox, B. T., Arridge, S. R. & Beard, P. C. 2007 Photoacoustic tomography with a limited-aperture planar sensor and a reverberant cavity. *Inverse Probl.* **23**, S95–S112. (doi:10.1088/0266-5611/23/6/S08)
57 Modgil, D., Anastasio, A. M., Wang, K. & LaRiviere, P. J. 2009 Image reconstruction in photoacoustic tomography with variable speed of sound using a higher order geometrical acoustics approximation. *Proc. SPIE* **7177**, A71771–A717718.
58 Burgholzer, P., Hofer, C., Paltauf, G., Haltmeier, M. & Scherzer, O. 2005 Thermoacoustic tomography with integrating area and line detectors. *IEEE Trans. Ultrason. Ferroelectr. Freq. Cont.* **52**, 1577–1583. (doi:10.1109/TUFFC.2005.1516030)
59 Haltmeier, M., Scherzer, O., Burgholzer, P. & Paltauf, G. 2004 Thermoacoustic computed tomography with large planar receivers. *Inverse Probl.* **20**, 1663–1673. (doi:10.1088/0266-5611/20/5/021)
60 Paltauf, G., Nuster, R., Haltmeier, M. & Burgholzer, P. 2007 Experimental evaluation of reconstruction algorithms for limited view photoacoustic tomography with line detectors. *Inverse Probl.* **23**, S81–S94. (doi:10.1088/0266-5611/23/6/S07)
61 Kruger, R. A., Kiser, W. L., Reinecke, D. R., Kruger, G. A. & Miller, K. D. 2003 Thermoacoustic Molecular Imaging of Small Animals. *Mol. Imag.* **2**, 113–123. (doi:10.1162/153535003322331993)
62 Brecht, H.-P., Su, R., Fronheiser, M., Ermilov, S. A., Conjusteau, A. & Oraevsky, A. 2009 Whole-body three-dimensional optoacoustic tomography system for small animals. *J. Biomed. Opt.* **14**, 064007. (doi:10.1117/1.3259361)
63 Wang, X., Pang, Y., Ku, G., Stoica, G. & Wang, L. V. 2003 Three-dimensional laser-induced photoacoustic tomography of mouse brain with the skin and skull intact. *Opt. Lett.* **28**, 1739–1741. (doi:10.1364/OL.28.001739)
64 Wang, X., Pang, Y., Ku, G., Xie, X., Stoica, G. & Wang, L. V. 2003 Noninvasive laser-induced photoacoustic tomography for structural and functional *in vivo* imaging of the brain. *Nat. Biotechnol.* **21**, 803–806. (doi:10.1038/nbt839)
65 Zhang, Q., Liu, Z., Carney, P. R., Yuan, Z., Chen, H., Roper, S. N. & Jiang, H. 2008 Non-invasive imaging of epileptic seizures *in vivo* using photoacoustic tomography. *Phys. Med. Biol.* **53**, 1921–1931. (doi:10.1088/0031-9155/53/7/008)
66 Yang, S., Xing, D., Zhou, Q., Xiang, L. & Lao, Y. 2007 Functional imaging of cerebrovascular activities in small animals using high-resolution photoacoustic tomography. *Med. Phys.* **34**, 3294–3301. (doi:10.1118/1.2757088)
67 Lao, Y., Xing, D., Yang, S. & Xiang, L. 2008 Noninvasive photoacoustic imaging of the developing vasculature during early tumor growth. *Phys. Med. Biol.* **53**, 4203–4212. (doi:10.1088/0031-9155/53/15/013)
68 Buehler, A., Herzog, E., Razansky, D. & Ntziachristos, V. 2010 Video rate optoacoustic tomography of mouse kidney perfusion. *Opt. Lett.* **35**, 2475–2477. (doi:10.1364/OL.35.002475)
69 Taruttis, A., Herzog, E., Razansky, D. & Ntziachristos, V. 2010 Real-time imaging of cardiovascular dynamics and circulating gold nanorods with multispectral optoacoustic tomography. *Opt. Express* **18**, 19592–19602. (doi:10.1364/OE.18.019592)
70 Li, C., Aguirre, A., Gamelin, J., Maurudis, A., Zhu, Q. & Wang, L. V. 2010 Real-time photoacoustic tomography of cortical hemodynamics in small animals. *J. Biomed. Opt.* **15**, 010509. (doi:10.1117/1.3302807)
71 Gamelin, J., Maurudis, A., Aguirre, A., Huang, F., Guo, P., Wang, L. V. & Zhu, Q. 2009 A real-time photoacoustic tomography system for small animals. *Opt. Express* **17**, 10489–10498. (doi:10.1364/OE.17.010489)
72 Gamelin, J., Aguirre, A., Maurudis, A., Huang, F., Castillo, D., Wang, L. V. & Zhu, Q. 2010 Curved array photoacoustic tomographic system for small animal imaging. *J. Biomed. Opt.* **13**, 024007. (doi:10.1117/1.2907157)
73 Song, K. H., Stoica, G. & Wang, L. V. 2006 *In vivo* three-dimensional photoacoustic tomography of a whole mouse head. *Opt. Lett.* **31**, 2453–2455. (doi:10.1364/OL.31.002453)
74 Pramanik, M., Ku, G., Li, C. & Wang, L. V. 2008 Design and evaluation of a novel breast cancer detection system combining both thermoacoustic (TA) and photoacoustic (PA) tomography. *Med. Phys.* **35**, 2218–2223. (doi:10.1118/1.2911157)
75 Ermilov, S. A., Khamapirad, T., Conjusteau, A., Leonard, M. H., Lacewell, R., Mehta, K., Miller, T. & Oraevsky, A. A. 2009 Laser optoacoustic imaging system for detection of breast cancer. *J. Biomed. Opt.* **14**, 024007. (doi:10.1117/1.3086616)
76 Wang, X., Chamberland, D. L. & Jamadar, A. D. 2007 Noninvasive photoacoustic tomography of human peripheral joints toward diagnosis of inflammatory arthritis. *Opt. Lett.* **32**, 3002–3004. (doi:10.1364/OL.32.003002)
77 Kruger, R. A., Kiser, W. L., Reinecke, D. R. & Kruger, G. 2003 Thermoacoustic computed tomography using a

conventional linear transducer array. *Med. Phys.* **30**, 856–860. (doi:10.1118/1.1565340)
78 Shah, J., Park, S., Aglyamov, S., Larson, T., Ma, L., Sokolov, K., Johnston, K., Milner, T. & Emelianov, S. Y. 2010 Photoacoustic imaging and temperature measurement for photothermal cancer therapy. *J. Biomed. Opt.* **13**, 034024. (doi:10.1117/1.2940362)
79 Fronheiser, M. P., Ermilov, S. A., Brecht, H.-P., Conjusteau, A., Su, R., Mehta, K. & Oraevsky, A. A. 2011 Real-time optoacoustic monitoring and three-dimensional mapping of a human arm vasculature. *J. Biomed. Opt.* **15**, 021305. (doi:10.1117/1.3370336)
80 Aguirre, A., Guo, P., Gamelin, J., Yan, S., Sanders, M. M., Brewer, M. & Zhu, Q. 2011 Coregistered three-dimensional ultrasound and photoacoustic imaging system for ovarian tissue characterization. *J. Biomed. Opt.* **14**, 054014. (doi:10.1117/1.3233916)
81 Ephrat, P., Needles, A., Bilan, C., Trujillo, A., Theodoropoulos, C., Hirson, D., Foster, S. & Visualsonics. 2010 *Photoacoustic imaging of Murine tumors using the Vevo® 2100 micro-ultrasound system* (*Visualsonics White Paper*).
82 Song, L., Maslov, K., Bitton, R., Shung, K. & Wang, L. V. 2008 Fast 3–D dark-field reflection-mode photoacoustic microscopy *in vivo* with a 30–MHz ultrasound linear array. *J. Biomed. Opt.* **13**, 1–10.
83 Song, L., Maslov, K., Shung, K. K. & Wang, L. V. 2010 Ultrasound-array-based real-time photoacoustic microscopy of human pulsatile dynamics *in vivo*. *J. Biomed. Opt.* **15**, 021303. (doi:10.1117/1.3333545)
84 Beard, P. C., Perennes, F. & Mills, T. N. 1999 Transduction mechanisms of the Fabry–Perot polymer film sensing concept for wideband ultrasound detection. *IEEE Trans. Ultrason. Ferroelect. Freq. Cont.* **46**, 1575–1582. (doi:10.1109/58.808883)
85 Zhang, E., Laufer, J. & Beard, P. 2008 Backward-mode multiwavelength photoacoustic scanner using a planar Fabry–Perot polymer film ultrasound sensor for high-resolution three-dimensional imaging of biological tissues. *Appl. Opt.* **47**, 561–577. (doi:10.1364/AO.47.000561)
86 1994. British Standard: Safety of laser products BS EN 60825–1.
87 Lamont, M. & Beard, P. C. 2006 2D imaging of ultrasound fields using a CCD array to detect the output of a Fabry–Perot polymer film sensor. *Electron. Lett.* **42**, 187–189.
88 Laufer, J., Johnson, P., Zhang, E., Treeby, B., Cox, B., Pedley, B. & Beard, P. 2011 *In vivo* longitudinal photoacoustic imaging of subcutaneous tumours in mice. *SPIE Proc.* **7899**, 789915. (doi:10.1117/12.876782)
89 Laufer, J., Zhang, E., Raivich, G. & Beard, P. 2009 Three-dimensional noninvasive imaging of the vasculature in the mouse brain using a high resolution photoacoustic scanner. *Appl. Opt.* **48**, D299–D306. (doi:10.1364/AO.48.00D299)
90 Laufer, J. G., Cleary, J. O., Zhang, E. Z., Lythgoe, M. F. & Beard, P. C. 2010 Photoacoustic imaging of vascular networks in transgenic mice. *Proc. SPIE* **7564**, 75641A. (doi:10.1117/12.842204)
91 Maslov, K., Stoica, G. & Wang, L. V. 2005 *In vivo* dark-field reflection-mode photoacoustic microscopy. *Opt. Lett.* **30**, 625–627. (doi:10.1364/OL.30.000625)
92 Zhang, H. F., Maslov, K., Stoica, G. & Wang, L. V. 2006 Functional photoacoustic microscopy for high-resolution and noninvasive *in vivo* imaging. *Nat. Biotechnol.* **24**, 848–851. (doi:10.1038/nbt1220)
93 Zhang, H. F., Maslov, K. & Wang, L. V. 2007 *In vivo* imaging of subcutaneous structures using functional photoacoustic microscopy. *Nat. Protocols* **2**, 797–804. (doi:10.1038/nprot.2007.108)
94 Favazza, C. P., Jassim, O., Cornelius, L. A. & Wang, L. V. 2011 *In vivo* photoacoustic microscopy of human cutaneous microvasculature and a nevus. *J. Biomed. Opt.* **16**, 016015. (doi:10.1117/1.3528661)
95 Favazza, C. P., Cornelius, L. A. & Wang, L. V. 2011 *In vivo* functional photoacoustic microscopy of cutaneous microvasculature in human skin. *J. Biomed. Opt.* **16**, 026004. (doi:10.1117/1.3536522)
96 Stein, E. W., Maslov, K. & Wang, L. V. 2009 Noninvasive, *in vivo* imaging of the mouse brain using photoacoustic microscopy. *J. Appl. Phys.* **105**, 102027. (doi:10.1063/1.3116134)
97 Song, K. H. & Wang, L. V. 2008 Noninvasive photoacoustic imaging of the thoracic cavity and the kidney in small and large animals. *Med. Phys.* **35**, 4524–4529. (doi:10.1118/1.2977534)
98 Wang, X., Chamberland, D. L. & Xi, G. 2008 Noninvasive reflection mode photoacoustic imaging through infant skull toward imaging of neonatal brains. *J. Neurosci. Methods* **168**, 412–421. (doi:10.1016/j.jneumeth.2007.11.007)
99 Shi, W., Kerr, S., Utkin, I., Ranasinghesagara, J., Pan, L., Godwal, Y., Zemp, R. J. & Fedosejevs, R. 2010 Optical resolution photoacoustic microscopy using novel high-repetition-rate passively Q-switched microchip and fiber lasers. *J. Biomed. Opt.* **15**, 056017. (doi:10.1117/1.3502661)
100 De la Zerda, A. *et al.* 2008 Carbon nanotubes as photoacoustic molecular imaging agents in living mice. *Nat. Nanotechnol.* **3**, 557–562. (doi:10.1038/nnano.2008.231)
101 Zhang, H. F., Maslov, K. & Wang, L. V. 2006 Functional photoacoustic microscopy for high-resolution and noninvasive *in vivo* imaging. *Nat. Biotechnol.* **24**, 848–851. (doi:10.1038/nbt1220)
102 Li, M.-L., Zhang, H. E., Maslov, K., Stoica, G. & Wang, L. V. 2006 Improved *in vivo* photoacoustic microscopy based on a virtual-detector concept. *Opt. Lett.* **31**, 474–476. (doi:10.1364/OL.31.000474)
103 Passler, K., Nuster, R., Gratt, S., Burgholzer, P., Berer, T. & Paltauf, G. 2010 Scanning acoustic-photoacoustic microscopy using axicon transducers. *Biomed. Opt. Express* **1**, 318–323. (doi:10.1364/BOE.1.000318)
104 Savateeva, E. V., Karabutov, A. A., Bell, B., Johnigan, R., Motamedi, M. & Oraevsky, A. A. 2000 Noninvasive detection and staging of oral cancer *in vivo* with confocal optoacoustic tomography. *Proc. SPIE* **3916**, 55–66. (doi:10.1117/12.386341)
105 Maslov, K., Zhang, H. F., Hu, S. & Wang, L. V. 2008 Optical-resolution photoacoustic microscopy for *in vivo* imaging of single capillaries. *Opt. Lett.* **33**, 929–931. (doi:10.1364/OL.33.000929)
106 Hu, S., Maslov, K. & Wang, L. V. 2009 *In vivo* functional chronic imaging of a small animal model using optical-resolution photoacoustic microscopy. *Med. Phys.* **36**, 2320–2323. (doi:10.1118/1.3137572)
107 Xie, Z., Jiao, S., Zhang, H. F. & Puliafito, C. A. 2009 Laser-scanning optical-resolution photoacoustic microscopy. *Opt. Lett.* **34**, 1771–1773. (doi:10.1364/OL.34.001771)
108 Hu, S., Yan, P., Maslov, K., Lee, J.-M. & Wang, L. V. 2009 Intravital imaging of amyloid plaques in a transgenic mouse model using optical-resolution photoacoustic microscopy. *Opt. Lett.* **34**, 3899–3901. (doi:10.1364/OL.34.003899)
109 Hu, S., Maslov, K. & Wang, L. H. V. 2009 Noninvasive label-free imaging of microhemodynamics by optical-resolution photoacoustic microscopy. *Opt. Express* **17**, 7688–7693. (doi:10.1364/OE.17.007688)

110 Liao, L.-D. *et al.* 2010 Imaging brain hemodynamic changes during rat forepaw electrical stimulation using functional photoacoustic microscopy. *NeuroImage* **52**, 562–570. (doi:10.1016/j.neuroimage.2010.03.065)

111 Shelton, R. L. & Applegate, B. E. 2010 Off-axis photoacoustic microscopy. *IEEE Trans. Bio-Med. Eng.* **57**, 1835–1838. (doi:10.1109/TBME.2010.2043103)

112 Shelton, R. L. & Applegate, B. E. 2010 Ultrahigh resolution photoacoustic microscopy via transient absorption. *Biomed. Opt.* **1**, 676–686. (doi:10.1364/BOE.1.000676)

113 Zhang, E. Z., Laufer, J., Povaay, B., Alex, A., Hofer, B., Drexler, W. & Beard, P. 2010 Multimodal simultaneous photoacoustic tomography, optical resolution microscopy, and OCT system. *Proc. SPIE* **7564**, 75640U. (doi:10.1117/12.841615)

114 Jiang, M., Zhang, X., Puliafito, C. A., Zhang, H. F. & Jiao, S. 2010 Adaptive optics photoacoustic microscopy. *Opt. Express* **18**, 21770–21776. (doi:10.1364/OE.18.021770)

115 Rao, B., Li, L., Maslov, K. & Wang, L. 2010 Hybrid-scanning optical-resolution photoacoustic microscopy for *in vivo* vasculature imaging. *Opt. Lett.* **35**, 1521–1523. (doi:10.1364/OL.35.001521)

116 Ku, G., Maslov, K., Li, L. & Wang, L. V. 2010 Photoacoustic microscopy with 2–microm transverse resolution. *J. Biomed. Opt.* **15**, 021302. (doi:10.1117/1.3339912)

117 Hu, S., Maslov, K., Tsytsarev, V. & Wang, L. V. 2011 Functional transcranial brain imaging by optical-resolution photoacoustic microscopy. *J. Biomed. Opt.* **14**, 040503. (doi:10.1117/1.3194136)

118 Hu, S., Maslov, K. & Wang, L. V. 2011 Second-generation optical-resolution photoacoustic microscopy with improved sensitivity and speed. *Opt. Lett.* **36**, 1134–1136. (doi:10.1364/OL.36.001134)

119 Jiao, S., Xie, Z., Zhang, H. F. & Puliafito, C. A. 2009 Simultaneous multimodal imaging with integrated photoacoustic microscopy and optical coherence tomography. *Opt. Lett.* **34**, 2961–2963. (doi:10.1364/OL.34.002961)

120 Jiao, S., Jiang, M., Hu, J., Fawzi, A., Zhou, Q., Shung, K. K., Puliafito, C. A. & Zhang, H. F. 2010 Photoacoustic ophthalmoscopy for *in vivo* retinal imaging. *Opt. Express* **18**, 3967–3972. (doi:10.1364/OE.18.003967)

121 Hu, S., Rao, B., Maslov, K. & Wang, L. V. 2010 Label-free photoacoustic ophthalmic angiography. *Opt. Lett.* **35**, 1–3. (doi:10.1364/OL.35.000001)

122 Yang, J.-M., Maslov, K., Yang, H.-C., Zhou, Q., Shung, K. K. & Wang, L. V. 2009 Photoacoustic endoscopy. *Opt. Lett.* **34**, 1591–1593. (doi:10.1364/OL.34.001591)

123 Karpiouk, A. B., Wang, B. & Emelianov, S. Y. 2010 Development of a catheter for combined intravascular ultrasound and photoacoustic imaging. *Rev. Sci. Instrum.* **81**, 01490. (doi:10.1063/1.3274197)

124 a Yaseen, M., Ermilov, S., Brecht, H.-P., Su, R., Conjusteau, A., Fronheiser, M., Bell, B., Motamedi, M. & a Oraevsky, A. 2010 Optoacoustic imaging of the prostate: development toward image-guided biopsy. *J. Biomed. Opt.* **15**, 021310. (doi:10.1117/1.3333548)

125 Hsieh, B.-Y., Chen, S.-L., Ling, T., Guo, L. J. & Li, P.-C. 2010 Integrated intravascular ultrasound and photoacoustic imaging scan head. *Opt. Lett.* **35**, 2892–2894. (doi:10.1364/OL.35.002892)

126 Yuan, Y., Yang, S. & Xing, D. 2010 Preclinical photoacoustic imaging endoscope based on acousto-optic coaxial system using ring transducer array. *Opt. Lett.* **35**, 2266–2268. (doi:10.1364/OL.35.002266)

127 Jansen, K., van der Steen, A. F. W., van Beusekom, H. M. M., Oosterhuis, J. W. & van Soest, G. 2011 Intravascular photoacoustic imaging of human coronary atherosclerosis. *Opt. Lett.* **36**, 597–599. (doi:10.1364/OL.36.000597)

128 Zhang, E. Z. & Beard, P. C. 2011 A miniature all-optical photoacoustic imaging probe. *Proc. SPIE* **7899**, 78991F. (doi:10.1117/12.874883)

129 Xi, L., Sun, J., Zhu, Y., Wu, L., Xie, H. & Jiang, H. 2010 Photoacoustic imaging based on MEMS mirror scanning. *Biomed. Opt. Express* **1**, 1278–1283. (doi:10.1364/BOE.1.001278)

130 Yang, J.-M., Favazza, C., Chen, R., Maslov, K., Cai, X., Zhou, Q., Shung, K. K. & Wang, L. V. 2011 Volumetric photoacoustic endoscopy of upper gastrointestinal tract: ultrasonic transducer technology development. *Proc. SPIE* **7899**, 78990D1–78990D6. (doi:10.1117/12.875377)

131 Allen, T. J. & Beard, P. C. 2009 Photoacoustic characterisation of vascular tissue at NIR wavelengths. *Proc. SPIE* **7177**, 71770A. (doi:10.1117/12.808777)

132 Allen, T. J., Hall, A., Dhillon, A., Owen, J. S. & Beard, P. C. 2010 Photoacoustic imaging of lipid rich plaques in human aorta. *Proc. SPIE* **7564**, 75640C. (doi:10.1117/12.842205)

133 Wray, S., Cope, M., Delpy, D. T., Wyatt, J. S. & Reynolds, E. O. R. 1988 Characterisation of the near-infrared absorption spectra of cytochrome-AA3 and haemoglobin for the non-invasive monitoring of cerebral oxygenation. *Biochim. Biophys. Acta* **933**, 184–192. (doi:10.1016/0005-2728(88)90069-2)

134 Wang, L. V. 2009 *Photoacoustic imaging and spectroscopy*, ch. 11.Boca Raton, FL: CRC Press.

135 Laufer, J., Elwell, C., Delpy, D. & Beard, P. 2005 In vitro measurements of absolute blood oxygen saturation using pulsed near-infrared photoacoustic spectroscopy: accuracy and resolution. *Phys. Med. Biol.* **50**, 4409–4428. (doi:10.1088/0031-9155/50/18/011)

136 Wang, X., Xie, X., Ku, G., Wang, L. V. & Stoica, G. 2006 Noninvasive imaging of hemoglobin concentration and oxygenation in the rat brain using high-resolution photoacoustic tomography. *J. Biomed. Opt.* **11**, 024015. (doi:10.1117/1.2192804)

137 Cox, B. T., Arridge, S. R. & Beard, P. C. 2009 Estimating chromophore distributions from multiwavelength photoacoustic images. *J. Opt. Soc. Am. A Opt. Image Sci. Vis.* **26**, 443–455. (doi:10.1364/JOSAA.26.000443)

138 Laufer, J., Cox, B., Zhang, E. & Beard, P. 2010 Quantitative determination of chromophore concentrations from 2D photoacoustic images using a nonlinear model-based inversion scheme. *Appl. Opt.* **49**, 1219–1233. (doi:10.1364/AO.49.001219)

139 Yin, L., Wang, Q., Zhang, Q. & Jiang, H. 2007 Tomographic imaging of absolute optical absorption coefficient in turbid media using combined photoacoustic and diffusing light measurements. *Opt. Lett.* **32**, 2556–2558. (doi:10.1364/OL.32.002556)

140 Bauer, A. Q., Nothdurft, R. E., Erpelding, T. N., Wang, L. V. & Culver, P. 2011 Quantitative high-resolution photoacoustic spectroscopy by combining photoacoustic imaging with diffuse optical tomography. *Proc. SPIE* **7899**, 789930. (doi:10.1117/12.875549)

141 Xiao, J., Yuan, Z., He, J. & Jiang, H. 2010 Quantitative multispectral photoacoustic tomography and wavelength optimization. *J. X-ray Sci. Technol.* **18**, 415–427.

142 Rajian, J. R., Carson, P. L. & Wang, X. 2009 Quantitative photoacoustic measurement of tissue optical absorption spectrum aided by an optical contrast agent. *Opt. Exp.* **17**, 4879–4889. (doi:10.1364/OE.17.004879)

143 Ranasinghesagara, J. C. & Zemp, R. J. 2010 Combined photoacoustic and oblique-incidence diffuse reflectance system for quantitative photoacoustic imaging in turbid media. *J. Biomed. Opt.* **15**, 046016. (doi:10.1117/1.3470336)

144 Beard, P. C. 2001. *Flow velocity measurements. UK Patent Application.* WO 03/0393.

145 Fang, H., Maslov, K. & Wang, L. V. 2007 Photoacoustic doppler effect from flowing small light-absorbing particles. *Phys. Rev. Lett.* **99**, 184501. (doi:10.1103/physRevlett.99.184501)

146 Fang, H., Maslov, K. & Wang, L. V. 2007 Photoacoustic Doppler flow measurement in optically scattering media. *Appl. Phys. Lett.* **91**, 264103. (doi:10.1063/1.2825569)

147 Sheinfeld, A., Gilead, S. & Eyal, A. 2010 Photoacoustic Doppler measurement of flow using tone burst excitation. *Opt. Exp.* **18**, 4212–4221. (doi:10.1364/OE.18.004212)

148 Sheinfeld, A., Gilead, S. & Eyal, A. 2010 Simultaneous spatial and spectral mapping of flow using photoacoustic Doppler measurement. *J. Biomed. Opt.* **15**, 066010. (doi:10.1117/1.3509113)

149 Brunker, J. & Beard, P. 2010 Pulsed photoacoustic Doppler flowmetry using a cross correlation method. *Proc. SPIE* **7564**, 756426. (doi:10.1117/12.841760)

150 Brunker, J. & Beard, P. 2011 Pulsed photoacoustic Doppler flow measurements in blood-mimicking phantoms. *Proc. SPIE* **7899**, 78991K. (doi:10.1117/12.874469)

151 a Hein, I. & O'Brien, W. R. 1993 Current time-domain methods for assessing tissue motion by analysis from reflected ultrasound echoes-a review. *IEEE Trans. Ultrason. Ferroelect. Freq. Control* **40**, 84–102. (doi:10.1109/58.212556)

152 Evans, D. & McDicken, W. 2000 *Doppler Ultrasound: physics, instrumentation and signal processing* 2nd ed. Chichester, UK: Wiley.

153 Yao, J. J. & Wang, L. H. V. 2010 Transverse flow imaging based on photoacoustic Doppler bandwidth broadening. *J. Biomed. Opt.* **15**, 021304.(doi:10.1117/1.3339953)

154 Yao, J., Maslov, K., Shi, Y., Taber, L. & Wang, L. 2010 *In vivo* photoacoustic imaging of transverse blood flow by using Doppler broadening of bandwidth. *Opt. Lett.* **35**, 1419–1421. (doi:10.1364/OL.35.001419)

155 Yao, J., Maslov, K. I. & Wang, L. V. 2011 Noninvasive quantification of metabolic rate of oxygen (MRO2) by photoacoustic microscopy. *Proc. SPIE* **7899**, 78990N. (doi:10.1117/12.874777)

156 Larina, I. V., Larin, K. V. & Esenaliev, R. O. 2005 Real-time optoacoustic monitoring of temperature in tissues. *J. Phys. D Appl. Phys.* **38**, 2633–2639. (doi:10.1088/0022-3727/38/15/015)

157 Schule, G., Huttmann, G., Framme, C., Roider, J. & Brinkmann, R. 2004 Noninvasive optoacoustic temperature determination at the fundus of the eye during laser irradiation. *J. Biomed. Opt.* **9**, 173–179. (doi:10.1117/1.1627338)

158 Pramanik, M. & Wang, L. V. 2010 Thermoacoustic and photoacoustic sensing of temperature. *J. Biomed. Opt.* **14**, 054024. (doi:10.1117/1.3247155)

159 Manohar, S., Kharine, A., van Hespen, J. C. G., Steenbergen, W. & van Leeuwen, T. G. 2005 The Twente Photoacoustic Mammoscope: system overview and performance. *Phys. Med. Biol.* **50**, 2543–2557. (doi:10.1088/0031-9155/50/11/007)

160 Manohar, S., Vaartjes, S. E., van Hespen, J. C. G., Klaase, J. M., van den Engh, F. M., Steenbergen, W. & van Leeuwen, T. G. 2007 Initial results of *in vivo* non-invasive cancer imaging in the human breast using near-infrared photoacoustics. *Opt. Express* **15**, 12277–12285. (doi:10.1364/OE.15.012277)

161 Piras, D., Steenbergen, W., van Leeuwen, T. G. & Manohar, S. G. 2010 Photoacoustic imaging of the breast using the twente photoacoustic mammoscope: present status and future perspectives. *IEEE J. Select. Topics Quantum Electron.* **16**, 730–739. (doi:10.1109/JSTQE.2009.2034870)

162 Song, K. H., Stein, E. W., Margenthaler, J. A. & Wang, L. V. 2008 Noninvasive photoacoustic identification of sentinel lymph nodes containing methylene blue *in vivo* in a rat model. *J. Biomed. Opt.* **13**, 054033. (doi:10.1117/1.2976427)

163 Kim, C., Song, K. H., Gao, F., Wang, L. V. & Wang, L. V. 2010 Sentinel lymph nodes and lymphatic vessels: noninvasive dual-modality *in vivo* mapping by using indocyanine green in rats—volumetric spectroscopic. *Radiology* **255**. 442–450. (doi:10.1148/radiol.10090281)

164 Nie, L. & Xing, D. 2008 Microwave-induced thermoacoustic scanning CT for high-contrast and noninvasive breast cancer imaging. *Med. Phys.* **35**, 4026–4032. (doi:10.1118/1.2966345)

165 Ku, G., Fornage, B. D., Jin, X., Xu, M., Hunt, K. K. & Wang, L. V. 2005 Thermoacoustic and photoacoustic tomography of thick biological tissues toward breast imaging. *Technol. Cancer Res. Treat.* **4**, 559–566.

166 Erpelding, T., Kim, C., Pramanik, M. & Jankovic, L. 2010 Sentinel lymph nodes in the rat: noninvasive photoacoustic and us imaging with a clinical US system. *Radiology* **256**, 102–110. (doi:10.1148/radiol.10091772)

167 Khokhlova, T. D., Pelivanov, I. M., Kozhushko, V. V., Zharinov, A. N., Solomatin, V. S. & Karabutov, A. 2007 Optoacoustic imaging of absorbing objects in a turbid medium: ultimate sensitivity and application to breast cancer diagnostics. *Appl. Opt.* **46**, 262–272. (doi:10.1364/AO.46.000262)

168 Zhang, H. F., Maslov, K. m, Soica, G. & Wang, L. V. 2006 Imaging accute thermal burns by photoacoustic microscopy. *J. Biomed. Opt.* **11**, 054031–054033. (doi:10.1117/1.2355667)

169 Yamazaki, M., Sato, S., Ashida, H., Saito, D., Okada, Y. & Obara, M. 2005 Measurement of burn depths in rats using multiwavelength photoacoustic depth profiling. *J. Biomed. Opt.* **10**, 064011. (doi:10.1117/1.2137287)

170 Oh, J.-T., Li, M.-L., Zhang, H. F., Maslov, K., Stoica, G. & Wang, L. V. 2010 Three-dimensional imaging of skin melanoma *in vivo* by dual-wavelength photoacoustic microscopy. *J. Biomed. Opt.* **11**, 34032. (doi:10.1117/1.2210907)

171 Wang, B., Su, J. L., Amirian, J., Litovsky, S. H., Smalling, R. & Emelianov, S. 2010 Detection of lipid in atherosclerotic vessels using ultrasound-guided spectroscopic intravascular photoacoustic imaging. *Opt. Express* **18**, 4889–4897. (doi:10.1364/OE.18.004889)

172 Wang, B., Yantsen, E., Larson, T., Karpiouk, A. B., Sethuraman, S., Su, J. L., Sokolov, K. & Emelianov, S. Y. 2009 Plasmonic intravascular photoacoustic imaging for detection of macrophages in atherosclerotic plaques. *Nano Lett.* **9**, 2212–2217. (doi:10.1021/nl801852e)

173 Su, J. L.-S., Wang, B. & Emelianov, S. Y. 2009 Photoacoustic imaging of coronary artery stents. *Opt. Express* **17**, 19894–19901. (doi:10.1364/OE.17.019894)

174 Karpiouk, A. B., Aglyamov, S. R., Mallidi, S., Shah, J., Scott, W. G., Rubin, J. M. & Emelianov, S. Y. 2010 Combined ultrasound and photoacoustic imaging to detect and stage deep vein thrombosis: phantom and *ex vivo*studies. *J. Biomed. Opt.* **13**, 054061. (doi:10.1117/1.2992175)

175 Iulia, M. G., Jimmy, S., Doug, Y., James, A., Richard, S. & Stanislav, E. 2011 Methodical study on plaque characterization using integrated vascular ultrasound, strain and spectroscopic photoacoustic imaging. *SPIE Proc.* **7899**, 789902.

176 Silverman, R. H., Kong, F., Chen, Y. C., Lloyd, H. O., Kim, H. H., Cannata, J. M., Shung, K. K. & Coleman, D. J. 2010 High-resolution photoacoustic imaging of ocular tissues. *Ultrasound Med. Biol.* **36**, 733–742. (doi:10.1016/j.ultrasmedbio.2010.02.006)

177 de la Zerda, A., Paulus, Y. M., Teed, R., Bodapati, S., Dollberg, Y., Khuri-Yakub, B. T., Blumenkranz, M. S., Moshfeghi, D. M. & Gambhir, S. S. 2010 Photoacoustic ocular imaging. *Opt. Lett.* **35**, 270–272. (doi:10.1364/OL.35.000270)

178 Bossy, E., Daoudi, K., Boccara, A. C., Tanter, M., Aubry, J. F., Montaldo, G. & Fink, M. 2006 Time reversal of photoacoustic waves. *Appl. Phys. Lett.* **89**, 184108. (doi:10.1063/1.2382732)

179 Funke, A. R., Aubry, J.-F., Fink, M., Boccara, A.-C. & Bossy, E. 2009 Photoacoustic guidance of high intensity focused ultrasound with selective optical contrasts and time-reversal. *Appl. Phys. Lett.* **94**, 054102. (doi:10.1063/1.3077018)

180 Funke, A. R. 2010 On the feasibility of photoacoustic guidance of high-intensity focused ultrasound.PhD thesis, ESPCI ParisTech, Université Pierre et Marie Curie, Paris, France.

181 Chitnis, P. V., Mamou, J., Mclaughlan, J., Murray, T. & Roy, R. A. 2009 Photoacoustic thermometry for therapeutic hyperthermia. *IEEE Ultrason. Symp.* 1757–1760.

182 Essenpreis, M. 1992 Thermally induced changes in optical properties of biological tissues. PhD thesis, University College London, London, UK.

183 Larin, K. V., Larina, I. V. & Esenaliev, R. O. 2005 Monitoring of tissue coagulation during thermotherapy using optoacoustic technique. *J. Phys. D Appl. Phys.* **38**, 2645–2653. (doi:10.1088/0022-3727/38/15/017)

184 Pelivanov, I., Sapozhnikov, O. & Khokhlova, A. A. 2006 Opto-acoustic diagnostics of the thermal action of high-intensity focused ultrasound on biological tissues: the possibility of its applications and model experiments. *Quant. Electron.* **36**, 1097–1102. (doi:10.1070/QE2006v036n12ABEH013261)

185 Chitnis, P. V., Brecht, H.-P., Su, R. & a Oraevsky, A. 2010 Feasibility of optoacoustic visualization of high-intensity focused ultrasound-induced thermal lesions in live tissue. *J. Biomed. Opt.* **15**, 021313. (doi:10.1117/1.3339977)

186 Cui, H. & Yang, X. 2010 *In vivo* imaging and treatment of solid tumor using integrated photoacoustic imaging and high intensity focused ultrasound system. *Med. Phys.* **37**, 4777–4781. (doi:10.1118/1.3480963)

187 Jin, X., Xu, Y., Wang, L. V., Fang, Y. R., Zanelli, C. I. & Howard, S. M. 2005 Imaging of high-intensity focused ultrasound-induced lesions in soft biological tissue using thermoacoustic tomography. *Med. Phys.* **32**, 5–11. (doi:10.1118/1.1829403)

188 Stein, E. W., Maslov, K. & Wang, L. V. 2010 Non-invasive, *in vivo* imaging of blood-oxygenation dynamics within the mouse brain using photoacoustic microscopy. *J. Biomed. Opt.* **14**, 020502. (doi:10.1117/1.3095799)

189 Ku, G., Wang, X., Xie, X., Stoica, G. & Wang, L. V. 2005 Imaging of tumor angiogenesis in rat brains *in vivo* by photoacoustic tomography. *Appl. Opt.* **44**, 770–775. (doi:10.1364/AO.44.000770)

190 Siphanto, R. I., Thumma, K. K., Kolkman, R. G. M., van Leeuwen, T. G., de Mul, F. F. M., van Neck, J. W., van Adrichem, L. N . A. & Steenbergen, W. 2005 Serial non-invasive photoacoustic imaging of neovascularization in tumor angiogenesis. *Opt. Express* **13**, 89–95. (doi:10.1364/OPEX.13.000089)

191 Kim, C. *et al.* 2010 *In vivo* molecular photoacoustic tomography of melanomas targeted by bioconjugated gold nanocages. *ACS Nano* **4**, 4559–4564. (doi:10.1021/nn100736c)

192 Razansky, D., Vinegoni, C. & Ntziachristos, V. 2007 Multispectral photoacoustic imaging of fluorochromes in small animals. *Opt. Lett.* **32**, 2891–2893. (doi:10.1364/OL.32.002891)

193 de la Zerda, A., Liu, Z., Bodapati, S., Teed, R., Vaithilingam, S., Khuri-Yakub, B. T., Chen, X., Dai, H. & Gambhir, S. S. 2010 Ultrahigh sensitivity carbon nanotube agents for photoacoustic molecular imaging in living mice. *Nano Lett.* **10**, 2168–2172. (doi:10.1021/nl100890d)

194 Li, P.-C., Wang, C.-R. C., Shieh, D.-B., Wei, C.-W., Liao, C.-K., Poe, C., Jhan, S., Ding, A.-A. & Wu, Y.-N. 2008 *In vivo* photoacoustic molecular imaging with simultaneous multiple selective targeting using antibody-conjugated gold nanorods. *Opt. Express* **16**, 18605–18615. (doi:10.1364/OE.16.018605)

195 Li, L., Zemp, R. J., Lungu, G., Stoica, G. & Wang, L. V. 2007 Photoacoustic imaging of lacZ gene expression *in vivo*. *J. Biomed. Opt.* **12**, 020504. (doi:10.1117/1.2717531)

196 Razansky, D., Distel, M., Vinegoni, C., Ma, R. & Perrimon, N. 2009 Multispectral opto-acoustic tomography of deep-seated fluorescent proteins *in vivo*. *Nat. Photon.* **3**, 412–417. (doi:10.1038/nphoton.2009.98)

197 Maxwell, A., Huang, S.-W., Ling, T., Kim, J.-S., Ashkenazi, S. & Guo, L. J. 2008 Polymer microring resonators for high-frequency ultrasound detection and imaging. *IEEE J. Select. Topics in Quantum Electron.* **14**, 191–197.

198 Wang, Y., Maslov, K., Zhang, Y., Hu, S., Yang, L., Xia, Y., Liu, J. & Wang, L. V. 2011 Fiber-laser-based photoacoustic microscopy and melanoma cell detection. *J. Biomed. Opt.* **16**, 011014. (doi:10.1117/1.3525643)

199 Allen, T. J., Shaiful, A., Zhang, E. Z., Laufer, J. G., Richardson, D. J. & Beard, P. C. 2011 Use of a pulsed fibre laser as an excitation source for photoacoustic tomography. *Proc SPIE* **7899**, 78991V. (doi:10.1117/12.875291)

200 Allen, T. J. & Beard, P. C. 2006 Pulsed NIR laser diode excitation system for biomedical photoacoustic imaging. *Opt. Lett.* **31**, 3462–3464.

201 Kolkman, R. G. M., Steenbergen, W. & Leeuwen, T. 2006 *In vivo* photoacoustic imaging of blood vessels with a pulsed laser diode. *Lasers Med. Sci.* **21**, 134–139. (doi:10.1007/s10103-006-0384-z)